動脈硬化の早期診断に向けた
アクチベータブルプローブのリポソーム DDS 製剤開発

Liposomal DDS of an activatable probe for optical diagnosis of atherosclerosis

本論文は 静岡県立大学大学院 薬食生命科学総合学府 薬学研究院 博士論文である

2019 年 3 月
March 2019

静岡県立大学大学院 薬食生命科学総合学府 薬学研究院
博士後期課程 薬食生命科学専攻

医薬生命化学講座

成田 雄大
Yudai Narita

Abbreviations

ApoE	apolipoprotein E
BSA	bovine serum albumin
CHOL	cholesterol
DDS	drug delivery system
DIC	differential interference contrast
DPPC	dipalmitoylphosphatidylcholine
DPPS	dipalmitoylphosphatidylserine
FACS	fluorescent activation cell sorter
FBS	fetal bovine serum
FDG	fluorodeoxyglucose
FSC	forward scatter
Hb	hemoglobin
HbO_2	oxyhemoglobin
HDL	high-density lipoprotein
ICG	indocyanine green
KO	knockout
LDL	low-density lipoprotein
MRI	magnetic resonance imaging
MSOT	multispectral optoacoustic tomography
NIRF	near-infrared fluorescence
NZW	New Zealand white
PA	photoacoustic
PBS	phosphate-buffered saline
PC	phosphatidylcholine
PDI	polydispersity index
PE	phycoerythrin
P-ICG2-PS-Lip	Peptide-ICG2-encapsulated phosphatidylserine liposome
PS	phosphatidylserine
R-P-ICG2-PS-Lip	Randomized Peptide-ICG2-encapsulated phosphatidylserine liposome
SPECT	single photon emission computed tomography
SSC	side scatter
TEM	transmission electron microscope
WHHL	Watanabe heritable hyperlipidemic

Contents

Introduction

Atherosclerosis is a primary disease with various thrombotic complications such as myocardial infarction and cerebral ischemic stroke [1], which are leading causes of death in the developed countries [2]. For preventing the onset of these acute clinical events, the early diagnosis of atherosclerosis and subsequent treatment are required. As shown in Figure 1, the atherosclerotic plaque is generally categorized into 2 types according to its qualitative characteristics [3,4]: in one type the plaque is infiltrated by active macrophages, making it prone to rupture and leading to a higher risk of atherosclerosis-induced ischemic vascular diseases than that for the stable plaque lacking such infiltration [5-7]. Thus, early detection of embolism-vulnerable atherosclerotic plaques is clinically important for risk management of thrombotic diseases.

The diagnosis of atherosclerosis has been performed by using a wide variety of molecular imaging modalities [8,9]. It has been reported that magnetic resonance imaging (MRI) and positron emission tomography (PET) are clinically useful for detecting

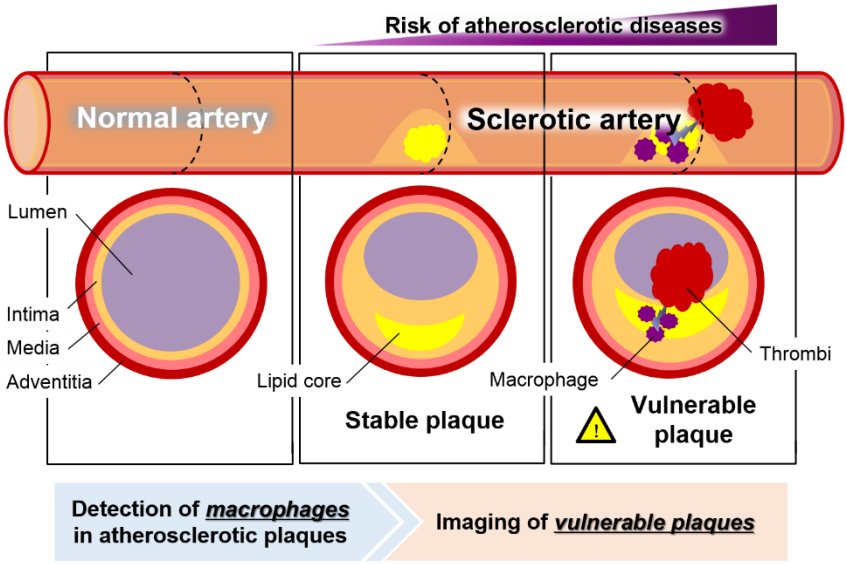

Figure 1. Qualitative characteristics of atherosclerotic plaques and strategy for imaging of atherosclerotic vulnerable plaque

atherosclerotic vulnerable plaques. The detection of coronary high-intensity plaques by non-contrast T1-weighted MRI has the potential for identifying the vulnerable regions [10-12]; and PET imaging using ^{18}F-flurodeoxyglucose (^{18}F-FDG) [13,14] or ^{18}F-sodium fluoride [15,16] can be used to evaluate the plaque vulnerability through the detection of vascular inflammation and microcalcification. Ogawa *et al.* previously reported that PET can detect the macrophage-dependent accumulation of ^{18}F-FDG in atherosclerotic plaques [17,18] and used it to evaluate the therapeutic effect of anti-inflammatory drugs on atherosclerosis [19]. Furthermore, they have already demonstrated that atherosclerotic lesions could be successfully visualized in both atherosclerotic model mice and rabbits by using single photon emission computed tomography (SPECT) imaging after injection of ^{111}In-loaded liposome [20]. However, these diagnostic modalities lack an easy operability, require large-scale facilities for installation of the imaging devices and technical skills for operation, and have a risk of radiation exposure during the scanning and medicinal preparation for both patients and operators (Figure 2). Although carotid

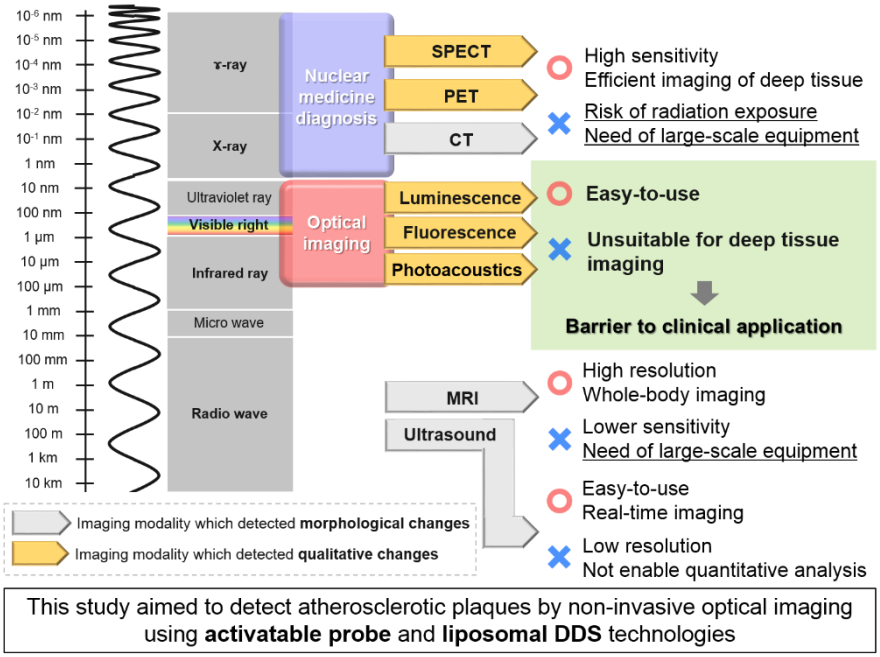

Figure 2. General properties of imaging modalities

ultrasound imaging is clinically performed to monitor the intimal thickness and the stenosis of carotid arteries as a non-invasive and easy-to-use method, such imaging is not able to detect qualitative changes in the plaque caused by inflammatory immune responses and/or enhanced enzyme activity.

Herein, to visualize easily the vulnerability of atherosclerotic plaques, I selected a near-infrared fluorescence (NIRF) imaging system, which is an easy-to-use imaging modality with a small-sized device and can be operated relatively easily without highly-advanced techniques. Notably, fluorescence imaging with an activatable probe that can be switched from "OFF" to "ON" to emit a fluorescent signal under certain circumstances [21] and has the potential to detect these signals at only targeted sites with reduced non-specific noises at non-targeted ones (Scheme 1), resulting in the acquisition of clear images at target sites with a high signal-to-noise ratio [22]. In this study, a novel NIRF activatable probe, Peptide-ICG2, designed by Ogawa *et al.* was used. The fluorescence of Peptide-ICG2 is quenched by conjugating it via a linker peptide to 2 molecules of an indocyanine green (ICG) fluorescent dye. The fluorescence of Peptide-ICG2 can become

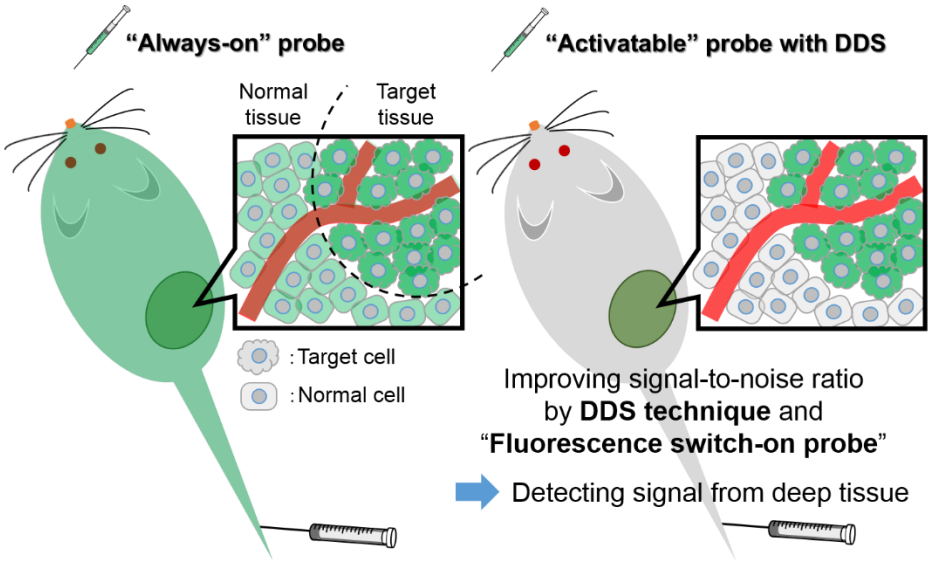

Scheme 1. Advantage of targeting delivery of activatable probe in optical imaging

detectable when the peptide has been cleaved by a lysosomal enzyme, cathepsin B, to release the quenching effect of the peptide. Because cathepsin B is highly expressed in the lysosomes of macrophages, the fluorescence can be dominantly imaged in the macrophages. In addition, cathepsin cysteine proteinases and matrix-metalloproteinases are secreted by macrophages and play an important role in the vulnerability of plaques by degrading collagen-rich cap matrix at the arterial intima [23-26]. In fact, focusing on these enzymatic activities, some groups have already performed fluorescence imaging of atherosclerotic lesions by using cathepsin activity-based probes [27-29]. Their findings indicate that cathepsin activity can be an indicator of vulnerability of the atherosclerotic plaques to an embolism.

On the other hand, to deliver the Peptide-ICG2 to the atherosclerotic plaques vulnerable to an embolism effectively, I prepared phosphatidylserine (PS)-containing liposome as a DDS carrier, which can target macrophages infiltrating into the plaques because PS receptors are highly expressed on the cell surface of the macrophage [30]. In this study, I prepared PS liposome encapsulating Peptide-ICG2 (P-ICG2-PS-Lip), and then evaluated their characteristics as a macrophage-targeted activatable NIRF probe.

Finally, I performed NIRF imaging using P-ICG2-PS-Lip in atherosclerosis model animals to confirm the usefulness of P-ICG2-PS-Lip for the diagnosis of atherosclerosis (Scheme 2). In addition, because ICG enables to be used as not only a fluorescence probe, but also a photoacoustic (PA) one, PA imaging was also performed for non-invasive detection of atherosclerotic plaques.

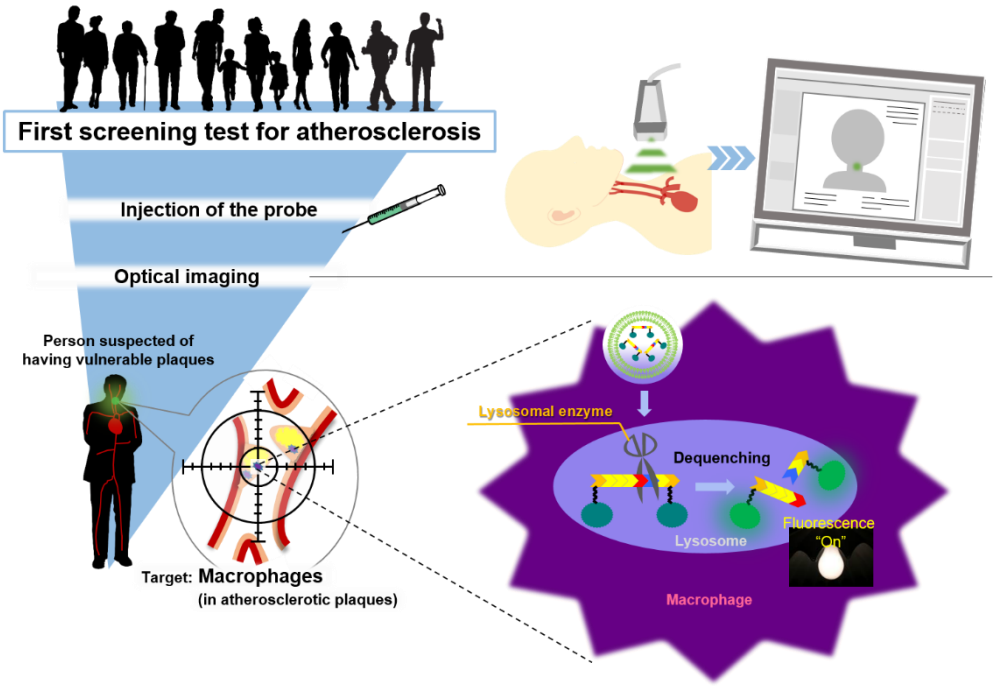

Scheme 2. Novel methodology of atherosclerosis diagnosis with P-ICG2-PS-Lip

Chapter 1. Synthesis of Peptide-ICG2 and preparation of PS liposome

To demonstrate atherosclerosis imaging with optical methodology, optical signal from the atherosclerotic lesion is needed to detect effectively. Therefore, synthesis of functional fluorescence probe and preparation of delivery carrier for the probe were tried for increase of the atherosclerotic plaque signals. In this chapter, Peptide-ICG2, the fluorescence activatable probe was designed, synthesized and evaluated whether fluorescence of ICG was detectable only when the probe was dequenched. Meanwhile, PS liposome, the delivery carrier was prepared and evaluated for targetability to macrophage cells *in vitro* and to atherosclerotic plaques *in vivo*.

1-1. Materials and Methods

1-1-1. Materials

2-[7-[1,3-Dihydro-1,1-dimethyl-3-(4-sulfobutyl)-2*H*-benzo[*e*]indol-2-ylidene]-1,3,5-heptatrienyl]-1,1-dimethyl-3-[5-(3-sulfosuccinimidyl)oxycarbonylpentyl]-1*H*-benzo[*e*]indolium, inner salt, sodium salt (ICG-sulfo-OSu) was purchased from Dojindo Laboratories (Kumamoto, Japan). Synthesis of *N*-terminally acetylated cathepsin B-cleavable (Ac-KGGGFLGK) peptide and the amino acid sequence-randomized (Ac-KGFGGGLK) peptide were outsourced to Japan Bio Services Co. (Saitama, Japan). 2-[7-[1,1-Dimethyl-3-(4-sulfobutyl)benz [e] indolin-2-ylidene]-1,3,5-heptatrienyl]-1,1-dimethyl-3-(4-sulfobutyl)-1*H*-benz [e] indolium hydroxide, inner salt, sodium salt (indocyanine green (ICG); Diagnogreen®) was purchased from Daiichi Sankyo Co. (Tokyo, Japan). Dipalmitoylphosphatidylcholine (DPPC) and cholesterol (CHOL) were supplied from Nippon Fine Chemical Co. (Hyogo, Japan). Dipalmitoylphosphatidylserine

(DPPS) was purchased from NOF Co. (Tokyo, Japan). 1,1′-Dioctadecyl-3,3,3′,3′-tetramethylindocarbocyanine perchlorate (DiI) and 3,3′-dioctadecyloxacarbocyanine perchlorate (DiO) were purchased from Thermo Fisher Scientific (Waltham, MA, USA). [^{3}H]Cholesteryl hexadecyl ether was purchased from PerkinElmer (Waltham, MA, USA).

1-1-2. Cell culture

Mouse macrophage-like RAW264 cells were purchased from the RIKEN Bioresource Center Cell Bank (Ibaraki, Japan); and mouse endothelial 2H11 cells, from the American Type Culture Collection (ATCC, Manassas, VA, USA). These cells were cultured in Dulbecco's modified Eagle's medium with high glucose (D-MEM; FUJIFILM Wako Pure Chemical Co.) supplemented with 10% heat-inactivated fetal bovine serum (FBS; HyClone, GE Healthcare UK, Buckinghamshire, England), 100-units/mL penicillin G (MP Biomedicals, Irvine, CA, USA), and 100-μg/mL streptomycin (MP Biomedicals) at 37ºC in a 5% CO_2 incubator.

1-1-3. Experimental animals

ApoE knockout (KO) B6.129P2-Apoetm1Unc/J mice (ApoE KO mice) were obtained from The Jackson Laboratory (Bar Harbor, ME, USA). The ApoE KO mice were fed a high-fat Clinton/Cybulsky diet with 1.25% cholesterol (Research Diets, New Brunswick, NJ, USA) from 6 weeks of age; and when they became 30 to 45 weeks old, they were used in *in vivo* experiments. Animal experiments were approved by either the Animal and Ethics Committee of University of Shizuoka or the Animal Care and Use Committee of the Hamamatsu University School of Medicine. The animals were cared for according to the Animal Facility Guidelines of the University of Shizuoka and Hamamatsu University School of Medicine.

1-1-4. Synthesis of Peptide-ICG2

Synthetic method of Peptide-ICG2 was established by Ogawa *et al*. In brief, ICG-sulfo-OSu was dissolved in anhydrous DMSO and Ac-KGGGFLGK peptide or randomized Ac-KGFGGGLK peptide was dissolved in PBS. ICG-sulfo-OSu was mixed with each peptide at molar ratio of ICG-sulfo-OSu / peptide = 2 / 1 in 0.1 M Na_2HPO_4 solution (pH 8.5) and incubated for 1 h in the dark at room temperature. After the reaction, the Peptide-ICG2 or randomized Peptide-ICG2 was purified by HPLC (LC20AC; Shimadzu Co., Kyoto Japan). HPLC analysis was performed with a mobile phase (acetonitrile / water = 45 / 55) at a flow rate of 0.5 mL/min, with separation on an ODS column (Cosmosil 5C18-AR-300, 4.6 x 250 mm; Nacalai Tesque, Inc., Kyoto, Japan) at 37ºC. The purified products were stored as a lyophilized powder at -20ºC.

To analyze a molecular weight of synthesized Peptide-ICG2, mass spectrometry analysis was performed. Peptide-ICG2 was dissolved with ethanol at 5 μg/mL as a concentration of Peptide-ICG2; and the mass spectrum was detected in positive ion mode by using an LCQ Fleet electrospray ionization mass spectrometer (Thermo Fisher Scientific Inc.).

1-1-5. Optical property of Peptide-ICG2

ICG and Peptide-ICG2 (1 μg/mL as ICG concentration) were dissolved in 20 mM sodium acetate buffer (pH 5.0), and the absorbance spectrum from wavelengths of 650 to 850 nm was measured with an Infinite M200 microplate reader (Tecan, Salzburg, Austria). The difference in fluorescence between ICG and Peptide-ICG2 was confirmed by measuring the fluorescence intensity at an excitation wavelength of 750 nm and emission wavelength of 845 nm by using the microplate reader.

To evaluate the fluorescence switch-on potential of Peptide-ICG2, Peptide-ICG2 or randomized Peptide-ICG2 (0.2 μg/mL as ICG, respectively) was mixed with 6 units/mL of human liver cathepsin B (Sigma-Aldrich) and incubated the mixture for 0, 1, 2 or 3 h at 37ºC in the presence or absence of 2 μg/mL of leupeptin (Sigma-Aldrich). The fluorescence intensity (Ex. 750 nm; Em. 845 nm) was measured by using the microplate reader after the incubation.

1-1-6. Preparation of PS liposome

The lipid compositions were DPPC, DPPS, and CHOL (1/1/1 as a molar ratio) for phosphatidylserine-containing liposome (PS liposome) and DPPC and CHOL (2/1 as a molar ratio) for phosphatidylcholine-containing liposome (PC liposome). The lipids dissolved in chloroform were dispersed in *tert*-butyl alcohol, lyophilized overnight, and subsequently hydrated with 120 mM sodium acetate solution. Then, the lipid solutions were freeze-thawed for 3 cycles, after which they were extruded through a 200-nm pore-sized polycarbonate membrane filter (Nuclepore, Cambridge, MA, USA) at 60ºC with a Lipex extruder (Transferra Nanosciences Inc., Burnaby, BC, Canada) to prepare PS and PC liposomes, respectively. For fluorescence labeling of the liposomes, DiI or DiO was mixed in the *tert*-butyl alcohol solution before the lyophilization. For assessing the influence of PS amounts of liposome on liposome uptake into macrophage, DiI-labeled liposomes that contained different amounts of PS at 10, 25, 30, 40 and 50% of total phospholipids were prepared. These lipid compositions were 1.8/0.2/1 (DPPC/DPPS/CHOL as molar ratio, below the same composition) for PS10% liposome, 1.5/0.5/1 for PS25% liposome, 1.4/0.6/1 for PS30% liposome, 1.2/0.8/1 for PS40% liposome and 1/1/1 for PS50% liposome respectively. For preparation of radiolabeled

liposomes, [^{3}H]cholesteryl hexadecyl ether was mixed with the other lipids in the *tert*-butyl alcohol solution before the lyophilization; and [^{3}H]-labeled PS liposomes and [^{3}H]-labeled PC liposomes were prepared as described above.

1-1-7. Cellular uptake of PS liposome

RAW264 (8 x 10^4 cells/well) or 2H11 cells (1 x 10^4 cells/well) were seeded onto the wells of a 24-well culture plate and pre-cultured overnight. DiI-labeled PS liposome or DiI-labeled PC liposome was incubated with the cells at 37 ºC for 1, 3, 6, 12 or 24 h. After having been washed, the cells were lysed with 0.1% sodium dodecyl sulfate-10 mM Tris-HCl buffer (pH 7.4). The fluorescence intensity of DiI (Ex. 549 nm; Em. 592 nm) in the lysates was measured by using the microplate reader. Targetability of PS10%, PS25%, PS30%, PS40%, and PS50% liposomes to the RAW264 cells was evaluated in a similar manner.

1-1-8. Fluorescence microscopic observation

RAW264 and 2H11 cells (1.5 x 10^4 cells/well, respectively) were seeded onto 35-mm culture dishes and co-cultured overnight. DiI-labeled PS liposome or DiI-labeled PC liposome was incubated at 37ºC for 6 h with the cells. After washing the cells with PBS, the cells were observed with a fluorescence microscope (IX71, OLYMPUS, Tokyo, Japan) and the fluorescence images were captured with a CCD camera (DP80, OLYMPUS). Exposure time of acquired images of DiI fluorescence were15 ms for PS liposome and 625 ms for PC liposome, respectively.

1-1-9. FACS analysis

Both RAW264 and 2H11 cells (7.5 x 10^4 cells/dish for each) were seeded onto

35-mm culture dishes and co-cultured overnight, after which DiO-labeled PS or PC liposome was added; and then the cells were incubated at 37ºC for 1 h. After having been washed with PBS containing 0.1% bovine serum albumin (BSA), the cells were treated with TruStain FcX (anti-CD16/32) antibody (BioLegend, San Diego, CA, USA), and then probed with anti-F4/80 antibody-phycoerythrin (PE) conjugate (BioLegend). Thereafter, the cells were scanned with a BD FACSCanto Ⅱ (BD Biosciences, Franklin Lakes, NJ, USA), and the obtained data were analyzed by use of a BD FACSDiva software (BD Biosciences).

1-1-10. Biodistribution of PS liposome in ApoE KO mice

[^{3}H]-labeled PS liposome or [^{3}H]-labeled PC liposome was intravenously injected into ApoE KO mice via a tail; and 24 h after the injection, the mice were sacrificed under anesthesia. The blood was collected and the plasma was separated by centrifugation (3,000 rpm, 20 min, 4ºC). The organs (heart, lung, liver, spleen, kidney and aorta) were dissected after cardiac perfusion with PBS. The collected samples were weighted and dissolved in Solvable (PerkinElmer) at 50ºC overnight. After having been sequentially added with 2-propanol (FUJIFILM Wako Pure Chemical Co.) and hydrogen peroxide (FUJIFILM Wako Pure Chemical Co.), the tissue lysates were mixed with Hionic-Fluor (PerkinElmer) for liquid scintillation. The radioactivity in the blood, the organs and the injected liposome solutions was measured with a liquid scintillation counter (LSC-7400, Hitachi Healthcare Manufacturing, Chiba, Japan).

1-2. Results

1-2-1. Preparation of Peptide-ICG2

Peptide-ICG2 was synthesized by amine coupling reaction of ICG-sulfo-OSu and Ac-KGGGFLGK peptide. Similarly, synthesis of randomized Peptide-ICG2 was performed using ICG-sulfo-OSu and randomized Ac-KGFGGGLK peptide (Figure 3A). Synthesized Peptide-ICG2 was analyzed by mass spectrometry; and a peak was detected at 1138.08 (m/z) in positive-ion mode of mass spectrum (Figure 3B). Then, to compare optical properties of Peptide-ICG2 to those of ICG, absorbance and fluorescence intensity were measured. Absorbance spectra of Peptide-ICG2 was obviously distinct from original that of ICG; and the distinctive absorbance maximum at the 785-nm wavelength of ICG was absent in absorbance spectra of Peptide-ICG2 (Figure 4A). The fluorescence intensity at 845 nm of Peptide-ICG2 excited by the wavelength at 750 nm was approximately 15 times lower than that of an equimolar amount of ICG (Figure 4B). On the other hand, fluorescence intensity of Peptide-ICG2 was increased with time of an incubation in the presence of cathepsin B. In addition, the fluorescence increase was inhibited by leupeptin, a cathepsin B inhibitor and the fluorescence intensity of randomized Peptide-ICG2 after the incubation with cathepsin B was lower than that of Peptide-ICG2 (Figure 4C).

(A)

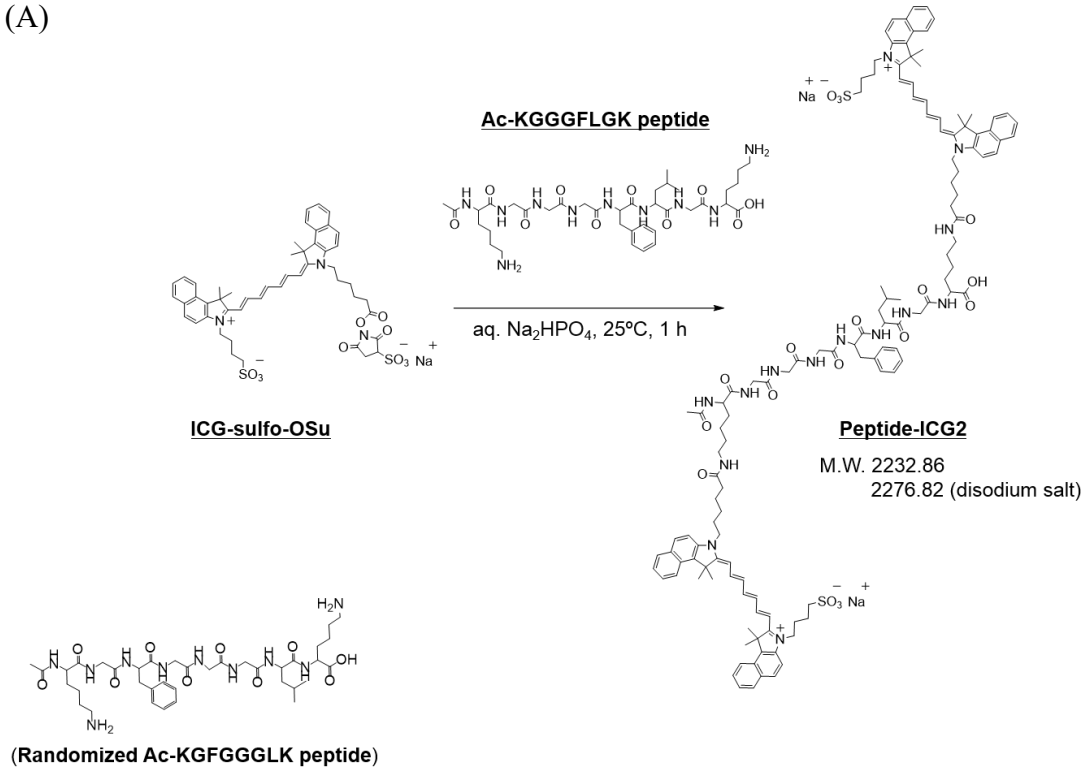

(B)

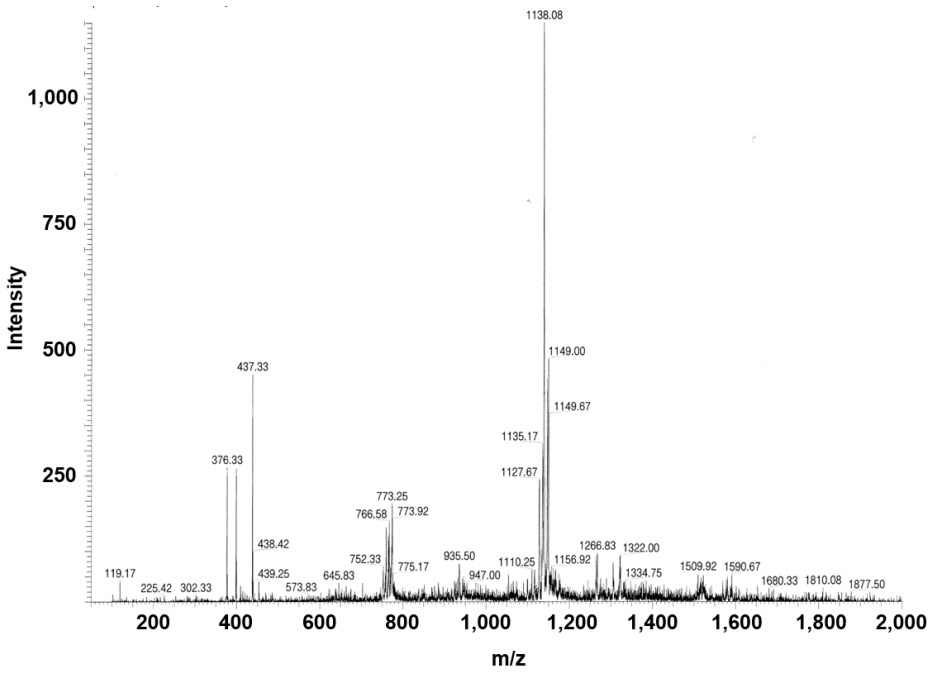

Figure 3. Synthesis of Peptide-ICG2

(A) Reaction scheme of Peptide-ICG2. Peptide-ICG2 was synthesized by amine coupling reaction of ICG-sulfo-OSu and Ac-KGGGFLGK peptide. Structure of randomized peptide (Ac-KGFGGGLK) was also shown. (B) The mass spectrum data of Peptide-ICG2. Peptide-ICG2 was analyzed in positive-ion mode of an ESI ion trap mass spectrometer.

(A)

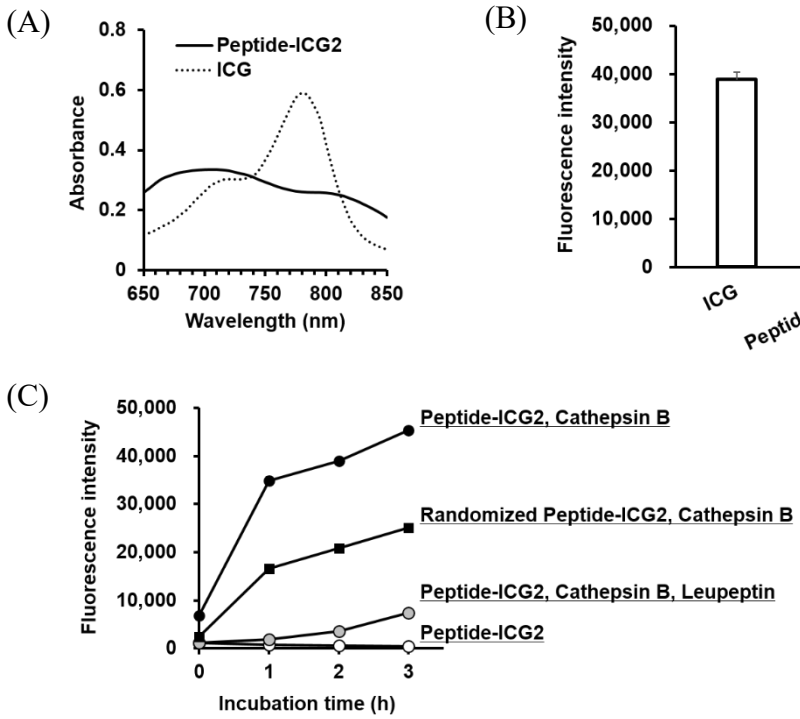

Figure 4. Optical properties of Peptide-ICG2
(A) Absorbance spectrum of Peptide-ICG2. Absorbance spectra of Peptide-ICG2 and ICG (1 μg/mL as ICG concentration) in 20 mM sodium acetate (pH 5.0) were obtained. (B) Quenched fluorescence of Peptide-ICG2. Fluorescence intensities of Peptide-ICG2 and ICG (Ex. wavelength at 750 nm, Em. wavelength at 845 nm) were measured with a microplate reader. Data are shown as the mean ± S.D. (n=6). (C) Fluorescence activation of Peptide-ICG2 by cathepsin B. Fluorescence activations of Peptide-ICG2 and randomized Peptide-ICG2 (0.2 μg/mL as ICG concentration) were plotted by measuring the fluorescence intensity at the indicated times during incubation with cathepsin B in the presence or absence of leupeptin. Data are shown as the mean ± S.D. (n=6).

1-2-2. PS-dependent uptake of liposome into macrophage cells

To detect embolism-vulnerable atherosclerotic plaques by fluorescence imaging, I focused on macrophages infiltrating into the plaques, because they play a crucial role in the development of atherosclerosis. To deliver Peptide-ICG2 to the macrophages in these plaques, I prepared PS liposome as a DDS carrier. In this study, I prepared PS liposome composed of DPPC/CHOL/DPPS (1/1/1 as a molar ratio) and evaluated their ability target macrophage cells in comparison with that of non-targeted PC liposome composed of

Table 1. Properties of the liposomes

	Particle size (nm)	PDI	ζ-Potential (mV)
DiI-labeled PC liposome	**186**	**0.150**	**+15.3**
DiI-labeled PS liposome	**190**	**0.177**	**-54.8**
DiO-labeled PC liposome	**191**	**0.068**	**-0.11**
DiO-labeled PS liposome	**180**	**0.129**	**-26.7**

ζ-Potentials of DiI-labeled liposomes were measured in ultrapure water. ζ-Potentials of DiO-labeled liposomes were measured in PBS.

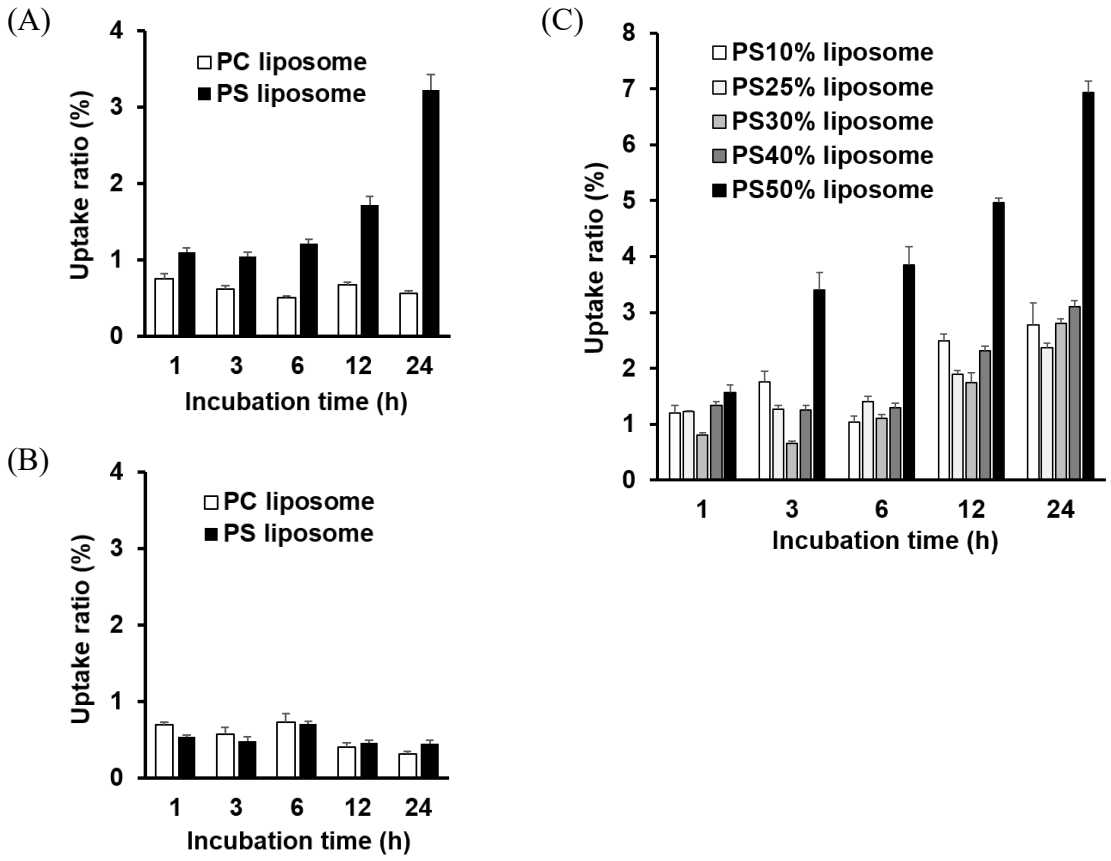

Figure 5. Uptake of PS liposome in macrophage cells
(A, B) Quantitative analysis of liposome uptake into macrophage cells. DiI-labeled PS or PC liposome (1mM as phospholipid concentration) was added to macrophage-like RAW264 cells (A) or mouse endothelial 2H11 cells (B), and the fluorescence intensity of DiI was measured at the indicated times after the start of incubation. The uptake ratio is presented as the amount of liposomes taken up as a percentage of the amount of liposome added. Data are shown as the mean ± S.D. (n=4). (C) Uptake of liposome contained different amounts of PS into RAW264 cells. DiI-labeled liposomes that contained different amounts of PS at 10, 25, 30, 40 and 50% of total phospholipids were incubated with RAW264 cells for 1, 3, 6, 12 and 24 h at 37ºC. Data are shown as the mean ± S.D. (n=4).

DPPC/CHOL (2/1 as a molar ratio). The physicochemical properties of DiI- and DiO-labeled PS liposomes and DiI- and DiO-labeled PC liposomes were respectively shown in Table 1. The particle size of the PS liposome was about 180 nm and the ζ-potential was quite negative. When the uptake of DiI-labeled PS liposome into mouse macrophage-like RAW264 cells was compared with that of PC liposome, the PS liposome showed higher uptake into RAW264 cells than the PC one, and the uptake amount increased in a time-dependent manner (Figure 5A). On the other hand, the uptake of PS liposome into mouse endothelial 2H11 cells was lower than that in RAW264 cells; and the uptake of PC liposome was not distinctly different between RAW264 and 2H11 cells (Figure 5B). Furthermore, to investigate the involvement of PS amount in the uptake into macrophage cells, a series of PS liposome that contained different amounts of PS from 0 to 50% of total phospholipids were prepared and the uptake of the liposomes into RAW264 cells was compared. As the result, PS liposome containing 50% PS showed remarkably higher uptake than the other PS liposomes (Figure 5C).

1-2-3. Targetability of PS liposome to macrophage cells

To evaluate the targeting specificity of PS liposome for macrophage cells in cultures of macrophage cells and endothelial cells, the uptake of DiI-labeled PS liposome or PC liposome in this co-culture system was observed with a fluorescence microscope. Fluorescence images indicated that the uptake of PS liposome was mainly observed in RAW264 cells, whereas PC liposome was taken up equally into both kinds of cells (Figure 6A). The amount of liposome uptake was then analyzed quantitatively by use of flow cytometry. As the result of preliminary FACS analysis, 2 cell populations (P1 and P2) were predictively detected in the co-culture system, and these populations could be

identified as F4/80-positive (P1) cells or F4/80-negative ones (P2), respectively,

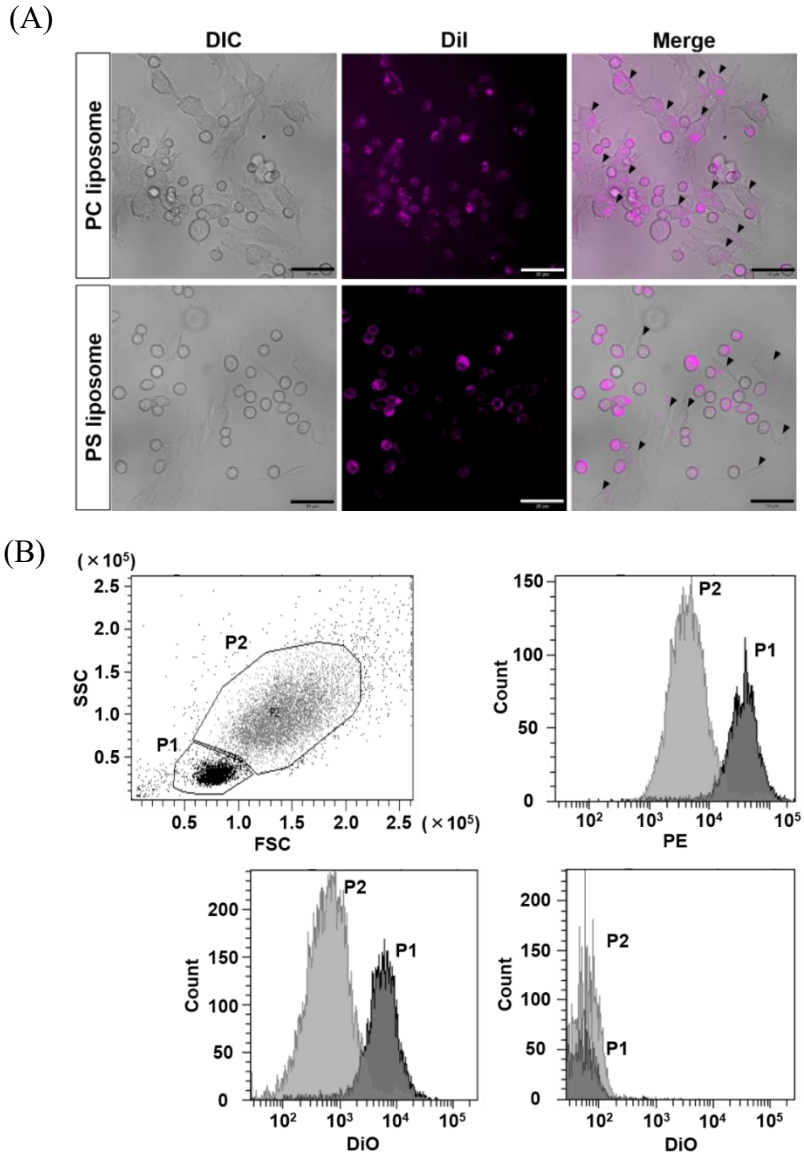

Figure 6. Selective targeting of macrophage cells by PS liposome
(A) Observation of macrophage targeting by PS liposome. DiI-labeled PS or PC liposome was added to co-cultures of RAW264 and 2H11 cells, and incubation was carried out for 6 h. Fluorescent images were obtained by fluorescence microscopy. Exposure time of scanning was 15 msec for PS liposome and 625 msec for PC one. Arrowheads show the location of 2H11 cells. Scale bars represent 50 μm. DIC: differential interference contrast. (B) FACS analysis of liposome uptake. RAW264 (7.5 x 10^4 cells/mL) and 2H11 (7.5 x 10^4 cells/mL) cells were co-cultured in 35-mm culture dishes overnight. DiI-labeled PS or PC liposome was incubated in the co-culture system for 1 h. After having been blocked with TruStain FcX (anti-CD16/32) antibody, the cells were probed with PE-conjugated anti-F4/80 antibody. The dot plot of forward scatter (FSC) vs. side scatter (SSC) (upper left chart) and the histogram of PE fluorescence (upper right chart) were obtained by FACS analysis with a BD FACSCanto II. The uptake of PS liposome (lower left chart) and PC liposome (lower right chart) into the cells was analyzed by the flow cytometry. Dark-colored or light-colored dot plot and histogram show the PE-positive (P1) or PE-negative (P2) population, respectively.

indicating P1 population was identified as macrophage cells. When DiO-labeled PS liposome was added to the co-culture system, their cell populations showed different uptakes of the liposome, with the PS liposome being significantly taken up into the F4/80-positive P1population. In addition, the uptake of PC liposome was much lower than that of PS one and not different between their populations (Figure 6B).

1-2-4. Biodistribution of PS liposome in ApoE KO mice

To elucidate targetability of PS liposome to atherosclerotic plaques, biodistribution of PS and PC liposomes containing radioactive tracer in ApoE KO mice was examined. While the radioactivity of PC liposome in the plasma at 24 h after the injection was 4 times higher than that of PS liposome, the accumulation of PS liposome in the liver was significantly higher than that of PC liposome. Accumulation in the spleen was decreased in PS liposome-treated mice. When the accumulation of the liposomes in the aorta was compared between PS and PC liposomes, PS liposome showed lower accumulation than PC liposome (Figure 7).

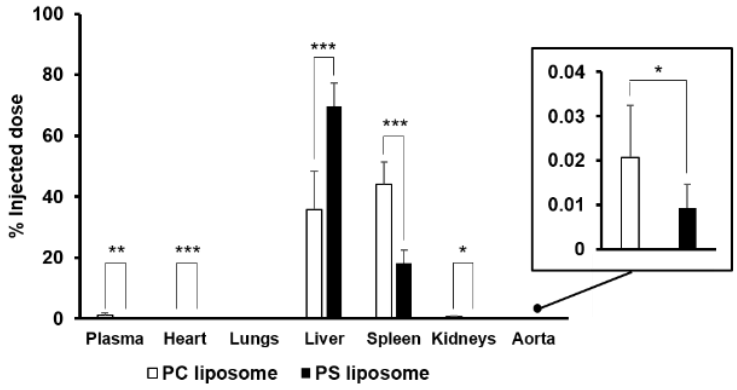

Figure 7. Biodistribution of PS liposome in atherosclerotic ApoE KO mice
[^{3}H]-labeled PS or PC liposome was intravenously injected to ApoE KO mice via the tail vein and allowed to circulate for 24 h. Then, the plasma and organ samples were prepared and the radioactivity was measured with a liquid scintillation counter. Data are shown as the mean ± S.D. (n=8-9). The significant differences are indicated as follows: *, $P < 0.05$; **, $P < 0.01$; and ***, $P < 0.001$.

1-3. Discussion

Activatable fluorescent probes have fluorescence switch-on sensors triggered under distinct circumstances and by certain factors such as pH [31], enzymes [32] and redox activity [33]. Therefore, the activatable probes are often used as indicators to understand the pH changes, enzymatic activity and O_2 concentration. Furthermore, they are applicable to *in vivo* fluorescence imaging for disease diagnosis, since disease sites are different circumstance from normal [34]. In the present study, Peptide-ICG2 was used as an activatable fluorescent probe sensed by cathepsin B activity and synthesized by an amine coupling reaction using both ICG-sulfo-OSu and *N*-terminally acetylated cathepsin B-cleavable linker peptide: Two ICG derivatives would covalently bound to lysine residues of the linker peptide. Amine coupling reaction is well known as one of bioconjugate techniques [35] and widely used to covalently bind biomolecule, such as peptide, protein, lipid, and so on, to other molecules. Therefore, I thought that the reaction would be suitable for synthesis of Peptide-ICG2. To evaluate whether Peptide-ICG2 is obtained as designed structure, synthesized Peptide-ICG2 was analyzed by mass spectrometry analysis. Since the peak of mass spectra was found at *m*/*z*=1138.08 (mass-to-charge ratio) in positive-ion mode: This *m*/*z* value was expected as the disodium salt

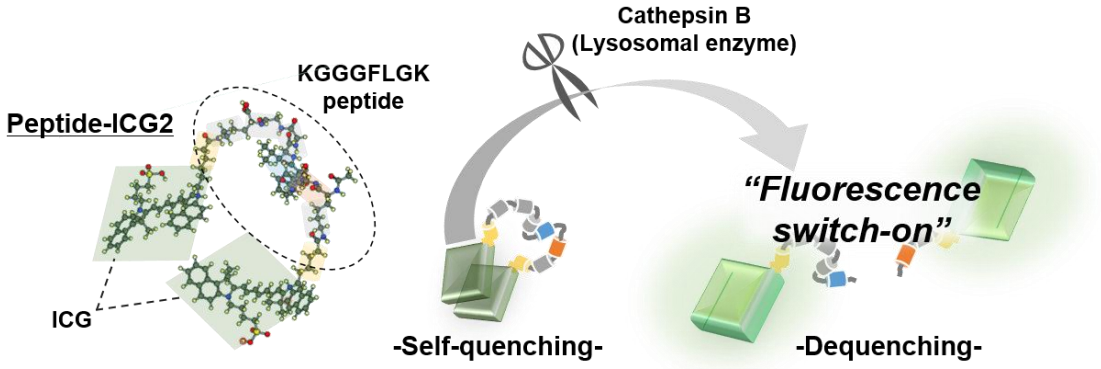

Scheme 3. Fluorescence activation of Peptide-ICG2

form of Peptide-ICG2 (Figure 3). The structural design and activatable function of Peptide-ICG2 are shown in Scheme 3. I assumed that the fluorescence of Peptide-ICG2 was quenched and that its fluorescence would be turned on by the switch function of cathepsin B. In fact, the optical properties of Peptide-ICG2 was obviously changed from those of original fluorescence dye, ICG; and the fluorescence of Peptide-ICG2 was quenched under normal condition and dequenched after addition of cathepsin B (Figure 4). These results indicate that Peptide-ICG2 fluorescence quenching had been induced by coupling ICGs with the peptide. It is well known that some fluorescent probes such as rhodamine- and BODIPY-derivatives form dimers and/or multimeric complexes at high concentrations [36,37] and that their fluorescence intensities are subsequently decreased by a quenching effect [38]. I speculated that the quenching mechanism of Peptide-ICG2 was caused by complex formation of 2 ICG molecules within a molecule: the linker peptide would produce a certain distance between these intramolecular ICGs, and then one ICG molecule could interact with another one by such π-π stacking. π-π stacked dyes displays different absorbance spectra from before complex formation; In fact, the absorbance spectrum of Peptide-ICG2 was obviously different from that of ICG (Figure 4A). Consequently, I succeeded in developing a near-infrared fluorescent probe specifically generated by cathepsin B.

Liposome is a lipid-based vesicle and widely used as a DDS carrier. As a biodistribution property of conventional liposome in the body, liposome accumulates in reticuloendothelial systems such as liver and spleen after the systemic injection, since the liposome is easily trapped by phagocytes such as liver Kupffer cells and macrophages. In addition, it was reported that liposome accumulates in atherosclerotic plaques [39]. These evidences promise that usage of liposome is convenient for specific delivery of the

fluorescent probe to macrophages infiltrating in the vulnerable plaques. Furthermore, phagocytic macrophages express a variety of PS-binding molecules and receptors, such as MGF-E8 [40], Protein S/Gas6 [41], and TIM4 [42]; and these macrophages recognize apoptotic cells, which have PS lipids exposed on their membrane surface, via PS-binding molecules and scavenger receptors expressed on the macrophage surface. These exposed PS molecules are sometimes referred to as the "eat-me signal" and constitute the clearance mechanism of apoptotic cells by macrophages [43-45]. Thus, PS liposome would be actively recognized by the infiltrating macrophages. In this study, I prepared PS liposome sized about 200 nm in a diameter for macrophage targeting, since some researchers have reported that liposome uptake into macrophage cells was increased with the particle size of liposomes [46,47] and that the accumulation of 400 nm-sized liposome in atherosclerotic region was lower than that of 200 nm-sized liposome [48]. Physicochemical properties of prepared liposomes were shown in Table 1 and PS liposome showed obviously negative surface charge, indicating that the negatively charged phospholipid, PS was certainly contained in the liposomal membrane. Then, the targetability of the prepared PS liposome to macrophage cells was investigated. In the experiments, I adopted the co-culture system of macrophage-like RAW264 and endothelial 2H11 cells to simulate the atherosclerotic vulnerable plaque environment, since macrophage cells and endothelial cells are involved in the formation of atherosclerotic vulnerable plaques [49]. As the results of liposome uptake assay, PS liposome was specifically taken up into macrophage-like RAW264 cells in the co-culture system (Figure 6).

To demonstrate the targetability of PS liposome to embolism-vulnerable atherosclerotic plaques, biodistribution analysis of PS liposome was carried out with

atherosclerotic model ApoE KO mice. The results indicated that PS liposome accumulated in the atherosclerotic aorta, but the accumulation amount was significantly lower than that of PC liposome regardless of macrophage-targeting function of PS (Figure 7). I thought the reason why PS liposome showed lower accumulation in the aorta was due to the shortened blood circulation time: PS liposome was easily trapped into the liver. In addition, the plaque formation at the arterial intima varied among different individuals and the accumulation of liposome was enhanced in the advanced atherosclerotic plaques. On the other hand, Ogawa *et al.* have previously demonstrated that the accumulation of 200 nm-sized PS liposome in atherosclerotic plaques was significantly higher than those of 100 nm-sized PS liposome and 200 nm-sized PC liposome [20]. These results and evidences promise the advantage of usage of PS liposome for macrophage targeting.

Consequently, I demonstrated that the PS liposome could selectively target macrophage cells through the active-targeting potential of PS to target macrophages, and be capable of a DDS carrier delivering the fluorescent probe to phagocytic macrophages residing in embolism-vulnerable atherosclerotic plaques (Scheme 4).

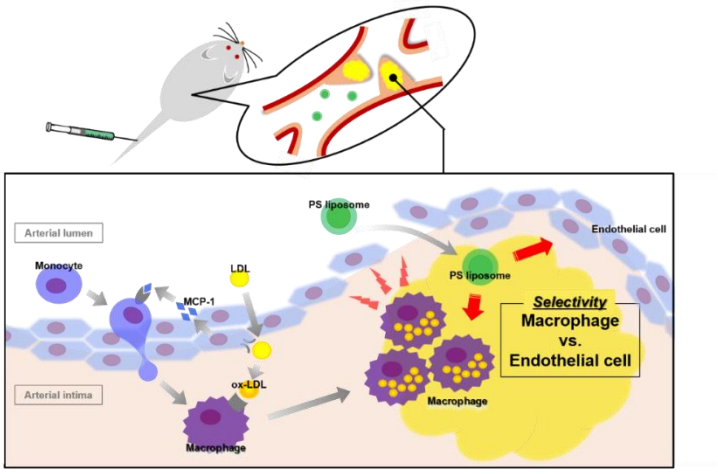

Scheme 4. Selective uptake of PS liposome into macrophage at atherosclerotic plaques

Chapter 2. Fluorescence activation of P-ICG2-PS-Lip in macrophage cells

Since the functional fluorescence probe and the delivery carrier were prepared in Chapter 1, P-ICG2-PS-Lip was prepared as an optical imaging agent for detection of atherosclerotic plaques in this Chapter. Prepared P-ICG2-PS-Lip was maintained at low level of fluorescence intensity in a buffer solution and in the present of serum protein. Additionally, P-ICG2-PS-Lip was evaluated if fluorescence switch-on would be induced at macrophage cells *in vitro* condition.

2-1. Materials and Methods

2-1-1. Materials

1,1'-Dioctadecyl-3,3,3',3'-tetramethylindotricarbocyanine iodide (DiR) were purchased from Thermo Fisher Scientific. The other chemical reagents were used as described in chapter 1.

2-1-2. Experimental animals

Male BALB/c mice (6 weeks old) and female ddY mice (6 weeks old) were purchased from Japan SLC (Shizuoka, Japan). Animal experiments were approved by either the Animal and Ethics Committee of University of Shizuoka or the Animal Care and Use Committee of the Hamamatsu University School of Medicine. The animals were cared for according to the Animal Facility Guidelines of the University of Shizuoka and Hamamatsu University School of Medicine.

2-1-3. Cell culture

Peritoneal macrophage cells were obtained as previously described [50]. In brief,

the ddY mice were intraperitoneally injected with 10% thioglycolate. Four days after the injection, the mice were sacrificed; intraperitoneally injected with PBS; and massaged around the abdomen to suspend the cells. Then, the macrophage cells were isolated from the peritoneal cavity by PBS lavage; and primary cultures of them were prepared in D-MEM (Sigma Aldrich, Saint Louis, MO, USA) containing heat-inactivated FBS, penicillin, and streptomycin at 37ºC in 5% CO_2.

2-1-4. Preparation of P-ICG2-PS-Lip

PS liposome and PC liposome were prepared as described in the section of 1-1-6. However, in the process of extrusion, 400-nm pore-sized polycarbonate membrane filter (Nuclepore) was used to prepare each liposome. For encapsulation of Peptide-ICG2 into the liposome, a remote loading method with acetate buffer was applied. In brief, PS liposome or PC liposome solution was dialyzed in ultrapure water at room temperature for at least 4 h and then resuspended in 120 mM citrate buffer (pH 5.0) after ultracentrifugation at 453,000 x *g*, for 15 min at 4ºC (CX120GXL, Hitachi, Tokyo, Japan). The liposome solutions were next mixed with Peptide-ICG2 and incubated for 1 h at 60ºC. Then, the solutions were purified by gel filtration chromatography (Sepharose 4 fast flow, GE Healthcare UK) for obtaining Peptide-ICG2-encapsulated PS liposome (P-ICG2-PS-Lip), Peptide-ICG2-encapsulated PC liposome (P-ICG2-Lip), and randomized Peptide-ICG2-encapsulated PS liposome (R-P-ICG2-PS-Lip). For preparation of DiR-labeled PS liposome, DiR was mixed in the *tert*-butyl alcohol solution before the lyophilization and the liposome solution was prepared as described in the section of 1-1-6.

2-1-5. Preparation of ICG-loaded liposome

The lipids composed of DPPC, DPPS and CHOL (1/1/1 as a molar ratio). The

lipids were dispersed in *tert*-butyl alcohol, lyophilized overnight, and subsequently hydrated with ICG solution (1.25 mg/mL as ICG concentration). Then, the liposome solution was freeze-thawed for 3 cycles, after which it was sequentially extruded through a 400-nm and 200-nm pore-sized polycarbonate membrane filters (Nuclepore) at 60ºC with a Lipex extruder to adjust the particle size. The liposome solution was purified by 3 times of ultracentrifugation for obtaining ICG-loaded PS liposome (ICG liposome).

2-1-6. Characteristics of P-ICG2-PS-Lip

Particle size and ζ-potential of liposome in water were measured by use of a Zetasizer Nano ZS (Malvern Instrument, Worcs, UK). The encapsulation ratio of Peptide-ICG2 in liposome was determined by measuring the fluorescence intensities of Peptide-ICG2 in the presence of 1% TritonX-100 (Sigma Aldrich) before and after purification, since fluorescence quenching of Peptide-ICG2 could be cancelled by addition of the detergent. Electron microscopic observation of P-ICG2-PS-Lip was performed with a HT7700 transmission electron microscope (TEM; Hitachi, Tokyo, Japan) after negative staining using 1% ammonium molybdate (FUJIFILM Wako Pure Chemical Co.). The fluorescent images of ICG, Peptide-ICG and P-ICG2-PS-Lip solutions were obtained with an IVIS Lumina fluorescence imaging apparatus (PerkinElmer).

2-1-7. Stability of P-ICG2-PS-Lip

P-ICG2-PS-Lip or Peptide-ICG2 mixed with empty PS liposome was incubated at 37ºC for 0, 1, 3, 6, 12 or 24 h in the presence of 90% FBS; and the fluorescence intensity of ICG (Ex. 750 nm; Em. 845 nm) was then measured with the microplate reader. To confirm the encapsulation stability of Peptide-ICG2, P-ICG2-PS-Lip or ICG liposome was incubated at 37ºC for 1 h in the presence of mouse serum, collected from the blood

of BALB/c mice. Then, the mixtures were separated into liposome fractions and serum protein fractions by gel filtration chromatography; and the fluorescence intensity of each fraction was measured in the presence of 1% TritonX-100 for P-ICG2-PS-Lip or in the absence of TritonX-100 for ICG liposome. On the other hands, to determine the liposome fraction and serum one, DiR-labeled PS liposome, or mouse serum was individually applied to the gel filtration chromatography; and the fluorescence intensity of DiR (Ex. 700 nn, Em. 790 nm), or the absorbance at 280 nm in each fraction was measured, respectively.

2-1-8. Fluorescence activation of P-ICG2-PS-Lip in RAW264 cells

RAW264 cells (1 x 10^4 cells/well) were seeded onto wells of a 96-well culture plate and pre-cultured overnight. P-ICG2-PS-Lip or P-ICG2-Lip was then added to the cells incubated at 37ºC for 0, 1, 3, 6, 12 and 24 h; and the fluorescence intensity of ICG (Ex. 750 nm; Em. 845 nm) was measured by using the microplate reader.

2-1-9. Time lapse observation of fluorescence activation of P-ICG2-PS-Lip

P-ICG2-PS-Lip or R-P-ICG2-PS-Lip was added to the murine peritoneal macrophage cells in FBS-containing medium and incubated at 37ºC (Thermo Plate, Tokai hit, Shizuoka, Japan) in the presence of 5% CO_2 (INU, Tokai hit). The fluorescence of ICG was observed in real time during the incubation with a time-lapse fluorescence microscope system (IX73, OLYMPUS).

2-1-10. Fluorescence activation of P-ICG2-PS-Lip in co-cultured RAW264 and 2H11 cells

To confirm cell specificity of fluorescence activation of P-ICG2-PS-Lip or R-P-

ICG2-PS-Lip, RAW264 (1.5 x 10^4 cells/well) and 2H11 (1.5 x 10^4 cells/well) cells were seeded onto 4-well culture slide glasses and then incubated with P-ICG2-PS-Lip or Peptide-ICG2 at 37ºC for 6 h. After mounting with PermaFlour (ThermoFisher Scientific Inc.), the fluorescence of ICG was observed with an IX71fluorescence microscope.

2-1-11. Intracellular distribution of P-ICG2-PS-Lip in RAW264 cells

To observe the intracellular distribution of ICG fluorescence, RAW264 cells (3 x 10^4 cells/well) were seeded onto a 4-well culture slide glass and then incubated with P-ICG2-PS-Lip at 37ºC for 6 h. Then, the lysosomes were stained with LysoTracker Green DND-26 (Life Technologies, Carlsbad, CA, USA) at 37ºC for 2 h, and the fluorescence were observed with the IX71 fluorescence microscope.

2-2. Results

2-2-1. Preparation of P-ICG2-PS-Lip

Because targeting potential of PS liposome to macrophage cells has been confirmed, next I encapsulated Peptide-ICG2 into PS liposome by a remote loading method as shown in Scheme 5, and the characteristics of which are summarized in Table 2. Similarly, the characteristics of ICG liposome was shown in Table 3. The average particle size of P-ICG2-PS-Lip was 180 nm, and the size distribution presented as a single peak (Figure 8A). Correspondingly, the TEM images also showed unilamellar vesicles of approximately 200 nm in size (Figure 8B).

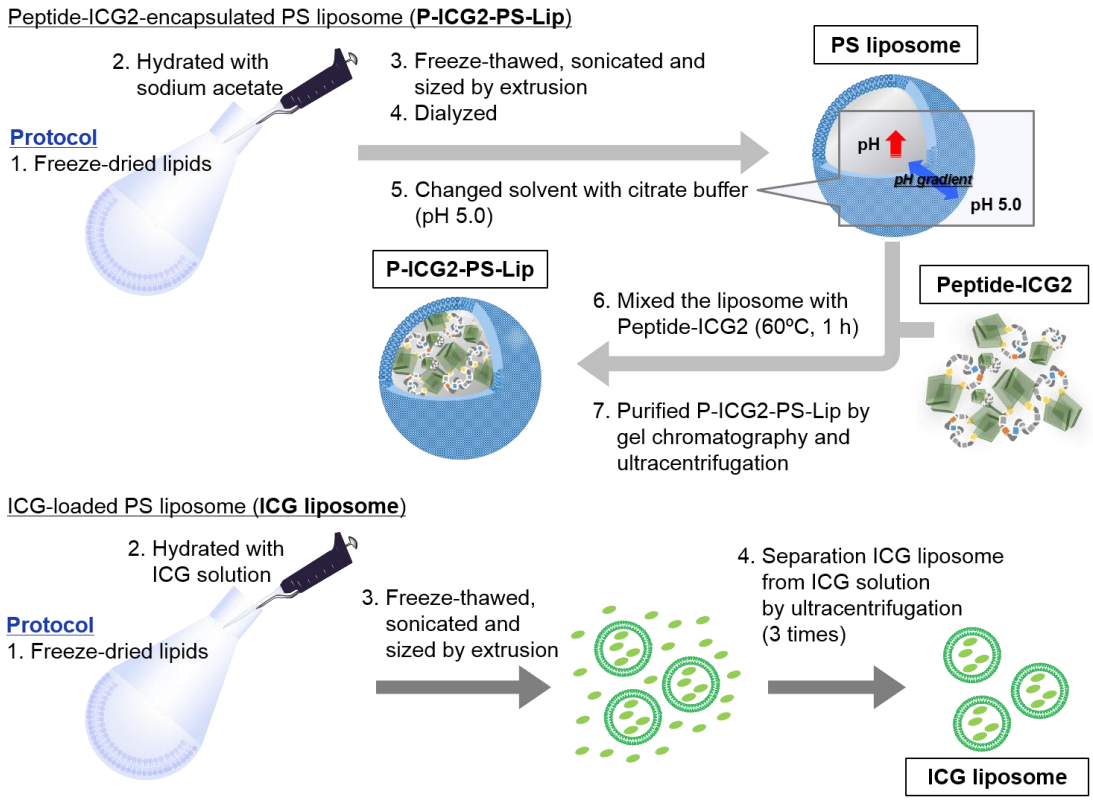

Scheme 5. Preparation of P-ICG2-PS-Lip and ICG liposome

Table 2. Properties of P-ICG2-PS-Lip

Particle size (nm)	PDI	ζ-Potential (mV)	Encapsulation of Peptide-ICG2 (%)
180 ± 14	0.077 ± 0.040	-67 ± 7	76 ± 15

Encapsulation ratio was calculated by measuring the fluorescence intensity (Ex. 750 nm; Em. 845 nm) in the presence of 1% TritonX-100 before and after purification of P-ICG2-PS-Lip. PDI: Polydispersity index.

Table 3. Properties of ICG liposome

Particle size (nm)	PDI	ζ-Potential (mV)	Encapsulation of ICG (%)
163 ± 8	0.096 ± 0.025	-69 ± 0.4	4.9 ± 1.2

Encapsulation ratio was calculated by measuring the absorbance at 795 nm in the presence of 1% TritonX-100. PDI: Polydispersity index.

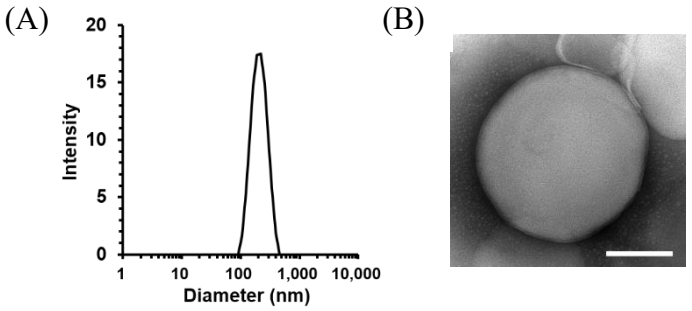

Figure 8. Particle size of P-ICG2-PS-Lip
(A) Size distribution of P-ICG2-PS-Lip. (B) Electron microscopic observation of P-ICG2-PS-Lip. The TEM image was obtained after negative staining with 1% ammonium molybdate. Scale bar represents 100 nm.

2-2-2. Stability of P-ICG2-PS-Lip in serum

To investigate whether quenching of Peptide-ICG2 would be maintained after encapsulation into liposome or not, I measured the fluorescence intensity of P-ICG2-PS-Lip. The fluorescence intensity of P-ICG2-PS-Lip remained at a low level and was similar to that of non-liposomal Peptide-ICG2 (Figure 9A). Then, to approximate the stability of fluorescence quenching of P-ICG2-PS-Lip *in vivo*, I measured their fluorescence intensity in the presence of FBS. As a result, P-ICG2-PS-Lip retained fluorescence quenching in FBS, although the fluorescence intensity of Peptide-ICG2 simply mixed with PS

liposome was immediately increased by FBS (Figure 9B). In addition, after P-ICG2-PS-Lip or ICG liposome was incubated with serum, the mixture was separated into liposome fractions and serum protein fractions and the fluorescence of each fraction was detected to confirm the release of the ingredients from the liposome. The fluorescence of ICG liposome was mostly detected at serum protein fractions after incubation with the mouse serum. On the other hand, the fluorescence of P-ICG2-PS-Lip was mostly detected at liposome fractions and trapping of the ingredients to serum proteins was little observed

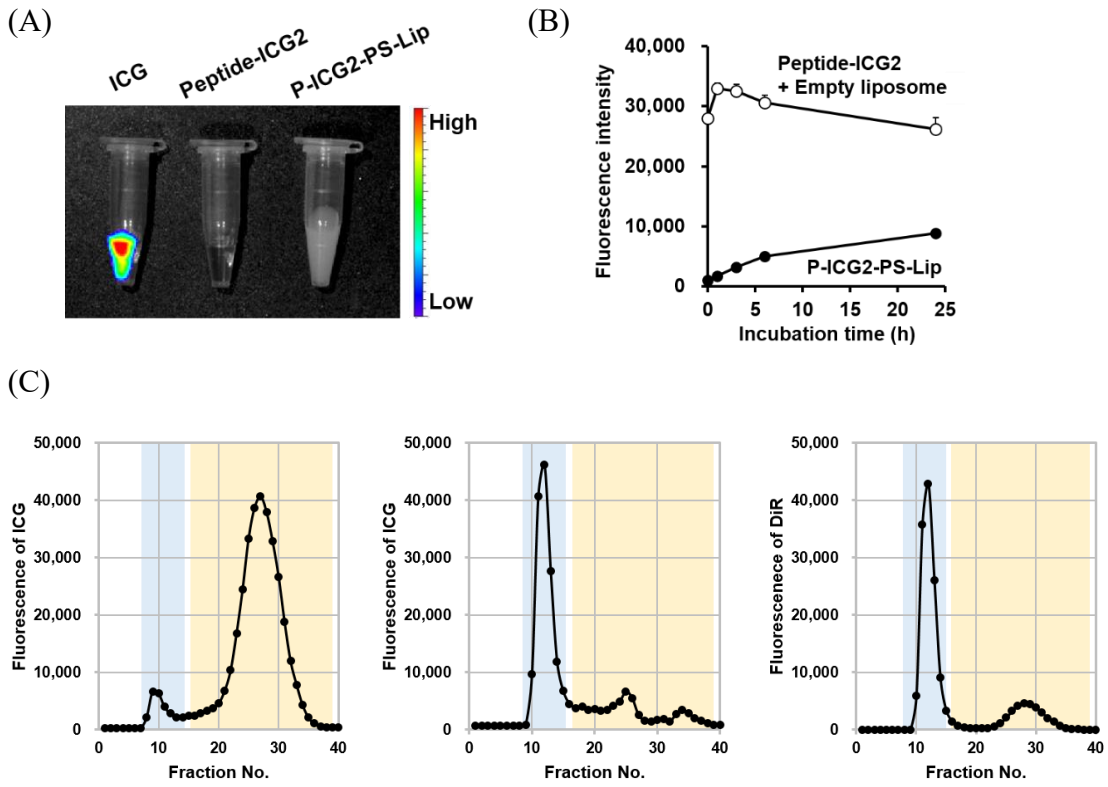

Figure 9. Fluorescence quenching stability of P-ICG2-PS-Lip in serum
(A) Fluorescence quenching of P-ICG2-PS-Lip in PBS. Fluorescence images of ICG, Peptide-ICG2 and P-ICG2-PS-Lip were obtained by scanning with an IVIS system. (B) Stability of fluorescence quenching of P-ICG2-PS-Lip in serum. Peptide-ICG2 or P-ICG2-PS-Lip was incubated at 37ºC in the presence of 90% FBS, and the fluorescence intensity was measured at indicated times during the incubation. (C) Encapsulation stability of Peptide-ICG2 in liposome. ICG liposome (left), P-ICG2-PS-Lip (Middle) or DiR-labeled liposome (right) was incubated with mouse serum at 37ºC for 1 h. Then, the gel filtration chromatography was carried. The fluorescence of ICG liposome or P-ICG2-PS-Lip in each fraction was measured in the absence, or presence of 1% TritonX-100, respectively. DiR-labeled liposome was used to determine the liposome fractions (from No. 8 to No. 15, blue-colored region). The serum protein fractions were determined by measuring the absorbance at 280 nm (from No.17 to No. 40, orange-colored region).

(Figure 9C).

2-2-3. Fluorescence activation of P-ICG2-PS-Lip in macrophage cells

To examine whether fluorescence activation of P-ICG2-PS-Lip would be induced in macrophage cells or not, I incubated PS-free P-ICG2-Lip or P-ICG2-PS-Lip with or without mouse macrophage-like RAW264 cells and monitored their fluorescence profile. As the result, the fluorescence intensity of P-ICG2-PS-Lip increased with incubation time in the presence of RAW264 cells, but not in their absence; although the fluorescence activation of PS-free P-ICG2-Lip was not observed despite the presence of the RAW264 cells (Figure 10A). Next, to investigate whether the fluorescence of P-ICG2-PS-Lip was activated by intracellular enzyme activity in macrophage cells or not, I added P-ICG2-PS-Lip to murine peritoneal macrophage cells and monitored activation of P-ICG2-PS-Lip fluorescence by live-cell imaging with a fluorescence microscope. The sequential fluorescence images showed that ICG fluorescence intensity seen in intracellular compartments grew with incubation time. Notably, the fluorescence in the culture medium containing FBS was little observed at even 6 h after the incubation (Figure 10B). On the other hand, when a similar experiment was carried out using R-P-ICG2-PS-Lip, the fluorescence activation was not observed (Figure 10C). To confirm the macrophage-specific fluorescence activation of P-ICG2-PS-Lip, I examined the ICG fluorescence in the co-culture system of RAW264 and mouse endothelial 2H11 cells after incubation with non-liposomal Peptide-ICG2 or P-ICG2-PS-Lip. The results indicated that ICG fluorescence was mainly observed in RAW264 cells after the incubation with P-ICG2-PS-Lip, whereas the fluorescence was clearly observed in both cells after the incubation with Peptide-ICG2 (Figure 10D). Furthermore, to investigate where the

fluorescence activation of P-ICG2-PS-Lip had occurred in macrophages, I examined the intracellular localization of ICG fluorescence in RAW264 cells. Fluorescence images showed that some hot spots of the fluorescence were dominantly co-localized with lysosomes stained by Lysotracker (Figure 10E).

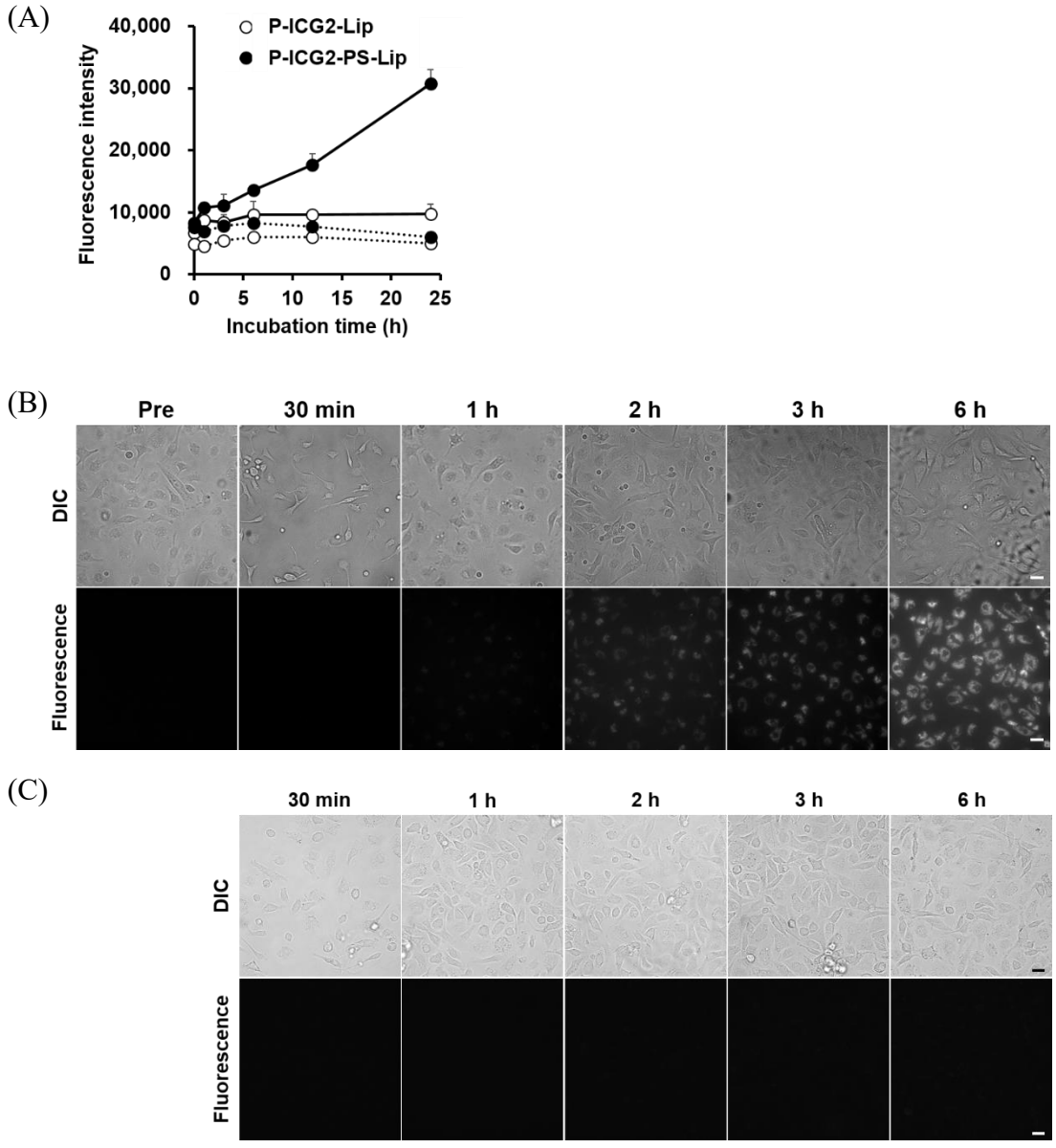

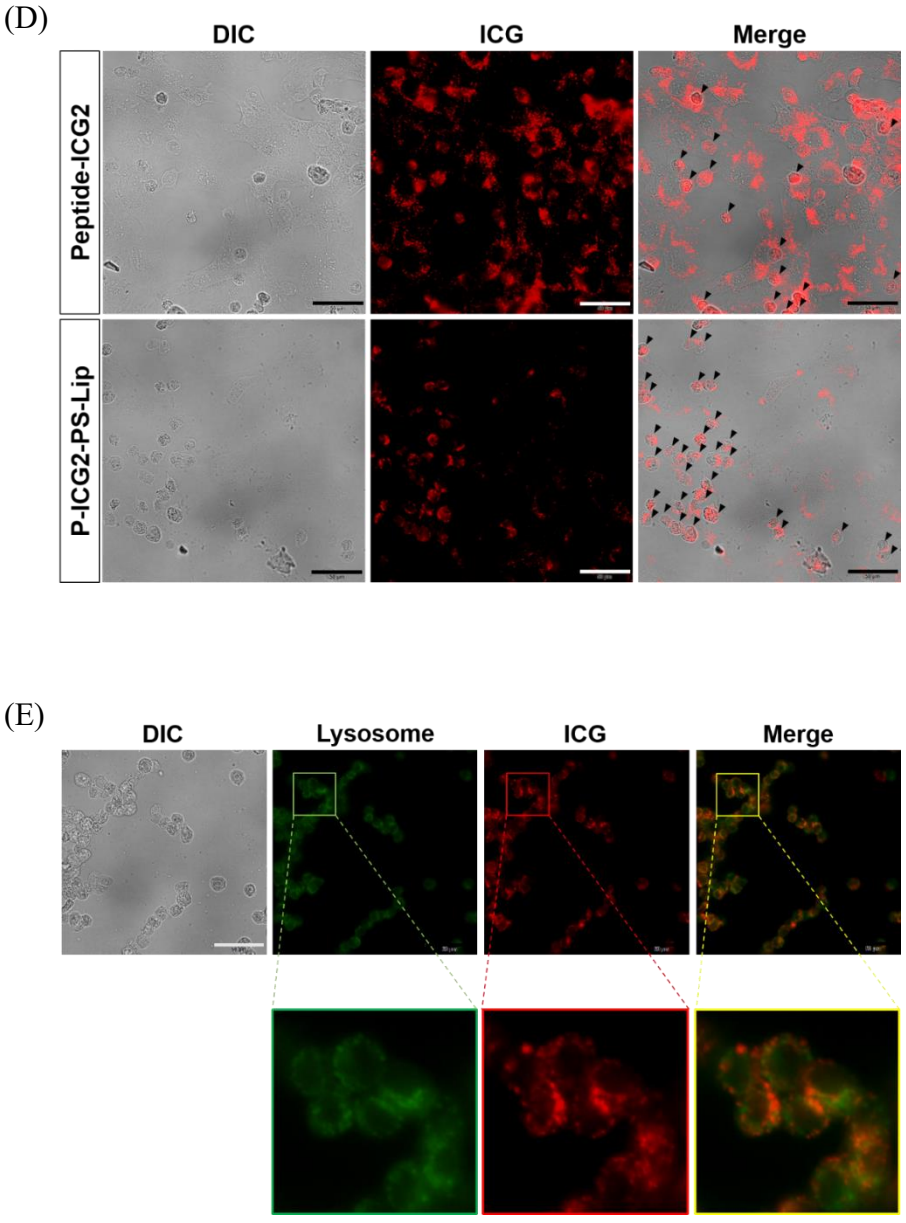

Figure 10. Fluorescence activation of P-ICG2-PS-Lip in macrophage cells
(A) Fluorescence activation of P-ICG2-PS-Lip in RAW264 cells. P-ICG2-Lip (open circle) or P-ICG2-PS-Lip (closed circle) was incubated with (solid line) or without (dotted line) RAW264 cells, and the fluorescence intensity of ICG was measured at the indicated times during the incubation. (B, C) Time-lapse observation of fluorescence activation in macrophage cells. P-ICG2-PS-Lip (B) or R-P-ICG2-PS-Lip (C) was incubated with murine peritoneal macrophage cells in FBS-containing medium, and fluorescence activation was monitored at the indicated times (without washing process) under a fluorescence microscope. Scale bars represent 20 μm. (D) Specific fluorescence switch-on of P-ICG2-PS-Lip in macrophage cells. Peptide-ICG2 or P-ICG2-PS-Lip was incubated in co-cultures of RAW264 and 2H11 cells. Six hours after the incubation, ICG fluorescence in the cells was observed. Arrowheads show the localization of RAW264 cells. Scale bars represent 50 μm. (E) Intracellular distribution of ICG fluorescence in macrophage cells. Six hours after incubation of P-ICG2-PS-Lip with RAW264 cells, the fluorescence of ICG (red) and that of Lysotracker (green) were observed. Scale bar represents 50 μm.

2-3. Discussion

As described in chapter 1, 200 nm-sized PS liposome was suitable for targeting the atherosclerotic lesions in terms of accumulation of the PS liposome in the plaques and uptake of that into macrophage cells. Therefore, I determined to prepare 200 nm-sized P-ICG2-PS-Lip. For preparing P-ICG2-PS-Lip, I first tried to encapsulate Peptide-ICG2 into PS liposome by a conventional hydration method, since some researchers have already prepared ICG-loaded liposome by using this method [51-53]. However, in a preliminary experiment using the hydration method, Peptide-ICG2 was not efficiently encapsulated into the liposomes, because physicochemical characteristics of Peptide-ICG2, such as molecular weight and electrical charge, would be different from that of ICG and negatively charged PS liposome would interrupt the encapsulation of the Peptide-ICG2. Therefore, the encapsulation of Peptide-ICG2 into PS liposome was performed by the remote-loading method with an acetate buffer (Scheme 5), which is well known as a method to encapsulate weakly acidic ingredients into liposomes [54,55]. In fact, I could encapsulate Peptide-ICG2 into PS liposome at an encapsulation ratio of over 75% (Table 2).

To evaluate *in vivo* utility of prepared P-ICG2-PS-Lip and the avoidance of non-specific fluorescence activation in bloodstream, the formulation stability of P-ICG2-PS-Lip in the serum was first examined. The results indicated that the fluorescence intensity of Peptide-ICG2 without encapsulation into liposome was immediately increased after mixing with the serum, suggesting that non-specific fluorescence activation of Peptide-ICG2 was brought by the interaction of Peptide-ICG2 with serum proteins such as α1-lipoprotein and albumin [56]. However, P-ICG2-PS-Lip was kept at low level of

fluorescence after incubation with serum. I believe that the non-specific fluorescence activation of Peptide-ICG2 was avoided by liposomalization and the stable encapsulation of Peptide-ICG2 in the liposome was achieved under neutral or weakly-basic condition of internal water phase of liposome produced by the remote-loading method using acetate buffer. It has been reported that the drug located in liposomal bilayer was easy to associate with serum proteins and the drug release from the liposome was quickly occurred in bloodstream [57]. On the other hand, liposomal doxorubicin, Doxil stably encapsulated the doxorubicin into internal water phase of liposome structure and protected from the association of the doxorubicin with serum proteins. The gel filtration chromatography after the incubation of P-ICG2-PS-Lip with serum resulted that the fluorescence of Peptide-ICG2 was observed in liposome fractions after the incubation of P-ICG2-PS-Lip with the serum (Figure 9C). These results mean that P-ICG2-PS-Lip had been successfully prepared and stably retained Peptide-ICG2 within while maintaining their fluorescence-quenching potential.

Considering the results from the fluorescence activation assay shown in Figure 4 and the liposome uptake assay in Figure 5A, I propose the speculation that macrophage-specific fluorescence activation would be achieved by macrophage-targeted delivery of Peptide-ICG2 carried by PS liposome. Thus, the fluorescence switch-on function of P-ICG2-PS-Lip in macrophage cells was examined. The results of fluorescence activation experiment with P-ICG2-PS-Lip in the co-cultured system of RAW264 and 2H11 cells showed that the fluorescence of P-ICG2-PS-Lip was preferentially dequenched in macrophage cells (Figure 10D). Besides, when P-ICG2-PS-Lip or R-P-ICG2-PS-Lip was incubated with murine peritoneal macrophages, the fluorescence activation was observed in only P-ICG2-PS-Lip-treated cells and the background fluorescence in the culture

medium was not observed (Figure 10B, C). These results suggest that the use of P-ICG2-PS-Lip can acquire clear fluorescence images in macrophage cells with a high signal-to-noise ratio. Moreover, to demonstrate the mechanism of fluorescence activation of P-ICG2-PS-Lip in the macrophage cells, the intracellular localization of ICG fluorescence in RAW264 cells was observed. As the result, the fluorescence of P-ICG2-PS-Lip had indeed been activated in the lysosomes. It is well known that most drug nanocarriers including liposome are taken up into cells through the endocytotic pathway, transferred to lysosomes following endosome formation, and degraded in them. In fact, Papahadjoupoulos *et al*. had already demonstrated that PS-containing liposome is taken up into macrophages via endocytosis [58]. As regards lysosomes, certain proteolytic enzymes such as cathepsin B are present in them, where biomolecules including proteins and peptides are digested for physiological metabolism [24,59,60]. Therefore, current accumulated data support my speculation that P-ICG2-PS-Lip were taken up into the macrophages by PS-mediated endocytosis, the encapsulated Peptide-ICG2 was released from the liposomes after disruption of the liposomes in the lysosomes, and the fluorescence was then activated in a cathepsin B-dependent manner. Consequently, I could demonstrate that P-ICG2-PS-Lip had the potential for switch-on fluorescence in macrophage cells.

Chapter 3. Optical imaging of atherosclerotic plaques using P-ICG2-PS-Lip

P-ICG2-PS-Lip demonstrated fluorescence switch function in macrophage cells as I had expected. Therefore, optical imaging with P-ICG2-PS-Lip was performed in some atherosclerotic model animals. P-ICG2-PS-Lip was injected to atherosclerotic mice and rabbit, then ex vivo imaging of aortae isolated from these animals was carried out to detect atherosclerotic lesion. In addition, *In vivo* fluorescence imaging and photoacoustic imaging with P-ICG2-PS-Lip-treated atherosclerotic monkeys was performed and evaluated whether atherosclerotic plaques at carotid arteries would be detect non-invasively.

3-1. Materials and Methods

3-1-1. Experimental animals

Watanabe heritable hyperlipidemic (WHHL) rabbit and normal New Zealand white (NZW) rabbit were purchased from Kitayama Labes Co. (Nagano, Japan). Cynomolgus monkeys were purchased from Eve Bioscience. (Wakayama, Japan); and fed with a banana-flavored high-fat diet containing 0.5% cholesterol and 6% corn oil (Research Diets) in order to develop atherosclerosis. Atherosclerosis progression in the monkeys were periodically monitored by MRI scan (Signa HDxt 3.0T; GE Healthcare UK) and the image of MR angiography were constructed. Measurements of biochemical values (total cholesterol, low-density lipoprotein (LDL) cholesterol, high-density lipoprotein (HDL) cholesterol and triglyceride) of the blood samples were commissioned to SRL, Inc. (Tokyo, Japan). All animal experiments were approved by the Animal Care and Use Committee of the Hamamatsu University School of Medicine. The animals were

cared for according to the Animal Facility Guidelines of the Hamamatsu University School of Medicine.

3-1-2. NIRF imaging of ApoE KO mice

P-ICG2-PS-Lip, R-P-ICG2-PS-Lip, ICG (approximately 20 μg/mouse as an ICG dose) or saline was intravenously injected into ApoE KO mice via a tail vein; and 24 h after the injection, the mice were sacrificed by excessive dose of sodium pentobarbital (Kyoritsu Seiyaku Corporation, Tokyo, Japan). Then, the aorta was dissected after cardiac perfusion with PBS and cut open to expose the atherosclerotic plaques. The fluorescence in the aortae was observed by using a Maestro2 imaging system (CRi Inc., Woburn, MA, USA). For ICG fluorescence imaging, a 700 - 770 nm band-pass filter was used for excitation; and a long-pass filter over 790 nm for emission. The fluorescence images were obtained by using the cube acquisition mode for spectral data obtained in 10-nm steps over the range of 780 - 950 nm emission wavelengths. After the fluorescence imaging, the aortae were stained with Oil Red O (Sigma Aldrich) for 30 min to confirm the presence of atherosclerotic plaques.

3-1-3. NIRF imaging of WHHL rabbit

A WHHL rabbit and normal NZW rabbit were intravenously injected with P-ICG2-PS-Lip (approximately 245 μg/rabbit as a Peptide-ICG2 dose) via a marginal ear vein under propofol (Aspen Japan K.K., Tokyo, Japan) anesthesia. Six hours after the injection, the rabbit was sacrificed by excessive dose of sodium pentobarbital and the aorta, aortic arch, and heart were then isolated after cardiac perfusion with saline. While dissecting the rabbit, fluorescence scanning was performed by a handheld near infrared fluorescence imager, pde-neo (Hamamatsu Photonics K.K., Shizuoka, Japan).

3-1-4. Immunostaining

The rabbit aorta was embedded in optical cutting temperature compound (Sakura, Finetek Japan Co., Tokyo, Japan) and frozen at -80ºC in a deep freezer. The frozen aorta was cut into 10-μm sections with a CM1850 cryostatic microtome (LEICA, Wetzlar, Deutschland). The aortic sections were incubated with PBS containing 3% BSA for blocking, and then probed with anti-CD68 mouse antibody (Abcam, Cambridge, UK) as the primary antibody followed by goat Alexa594-conjugated anti-mouse antibody as the secondary antibody (Thermo Fisher Scientific) for macrophage staining. After mounting with ProLong containing DAPI (Thermo Fisher Scientific), the sections were observed with the IX73 fluorescence microscope.

3-1-5. NIRF imaging of atherosclerotic model monkeys

Cynomolgus monkeys were intravenously injected with P-ICG2-PS-Lip or ICG liposome via a femoral vein under anesthesia using ketamine (Daiichi Sankyo) / xylazine for inducing hyponogenesis and 1.5% isoflurane (Pfizer Inc., NY, USA) for continual anethesia. Just after and 6 h after the injection, the ICG fluorescence at cervical region of the monkeys were scanned with a pde-neo alone (Method 1), or the pde-neo following excitation by a high power NIR light laser (Hamamatsu Photonics K.K.) (Method 2). After the *in vivo* imaging, the monkeys were sacrificed by excessive dose of anesthetic agents; the aorta, aortic arch, heart and, right and left carotid arteries were isolated following the blood perfused with saline; and fluorescence scanning of those organs was performed by using the pde-neo imager.

3-1-6. PA imaging in ApoE KO mice

ApoE KO mice dehaired by depilatory cream (Reckitt Benckiser, Berkshire, UK) were intravenously injected with P-ICG2-PS-Lip (approximately 10 μg as a Peptide-ICG2 dose) via a tail vein and 24 h after the injection, whole-body PA scan of the mice immersed in ultrasound gel was performed under 1.5% isoflurane anesthesia by a multispectral optoacoustic tomography (MSOT in Vision 256FT; iThera Medical, Munich, Deutschland) equipped with a TomoARC detector. The PA images were obtained by the reference to the PA spectral data of ICG, hemoglobin (Hb) and oxyhemoglobin (HbO_2).

3-1-7. PA imaging in atherosclerotic model monkeys

The atherosclerotic monkeys (25 months after the start of high-fat diet feeding) were intravenously injected with P-ICG2-PS-Lip (approximately 290 μg as a Peptide-ICG2 dose) via a femoral vein under ketamine / xylazine anesthesia. PA imaging scans at cervical region of the monkeys were non-invasively performed under 1.5% isoflurane anesthesia at 3 h after the injection by using the MSOT imaging system equipped with a handheld MSOT detector. After the *in vivo* imaging, the monkeys were sacrificed by excessive dose of anesthetic agent; the aorta, aortic arch, right and left carotid arteries were isolated following the blood perfusion with saline; and *ex vivo* imaging of the aorta and carotid arteries was performed with a MSOT imaging system.

3-2. Results

3-2-1. NIRF imaging of atherosclerotic plaques in ApoE KO mice with P-ICG2-PS-Lip

P-ICG2-PS-Lip was intravenously injected into the ApoE KO mice via a tail vein; and 24 h later, ICG fluorescence in the isolated aorta was scanned by use of Maestro2. As the result, ICG fluorescence signals were strongly detected at the aortae of P-ICG2-PS-Lip-treated ApoE KO mice, where the fluorescence was observed at lipid-rich blood vessel walls, but not at the normal regions (Figure 11A). When the aortae were stained with Oil Red O for determining the positions of atherosclerotic plaques, the ICG-

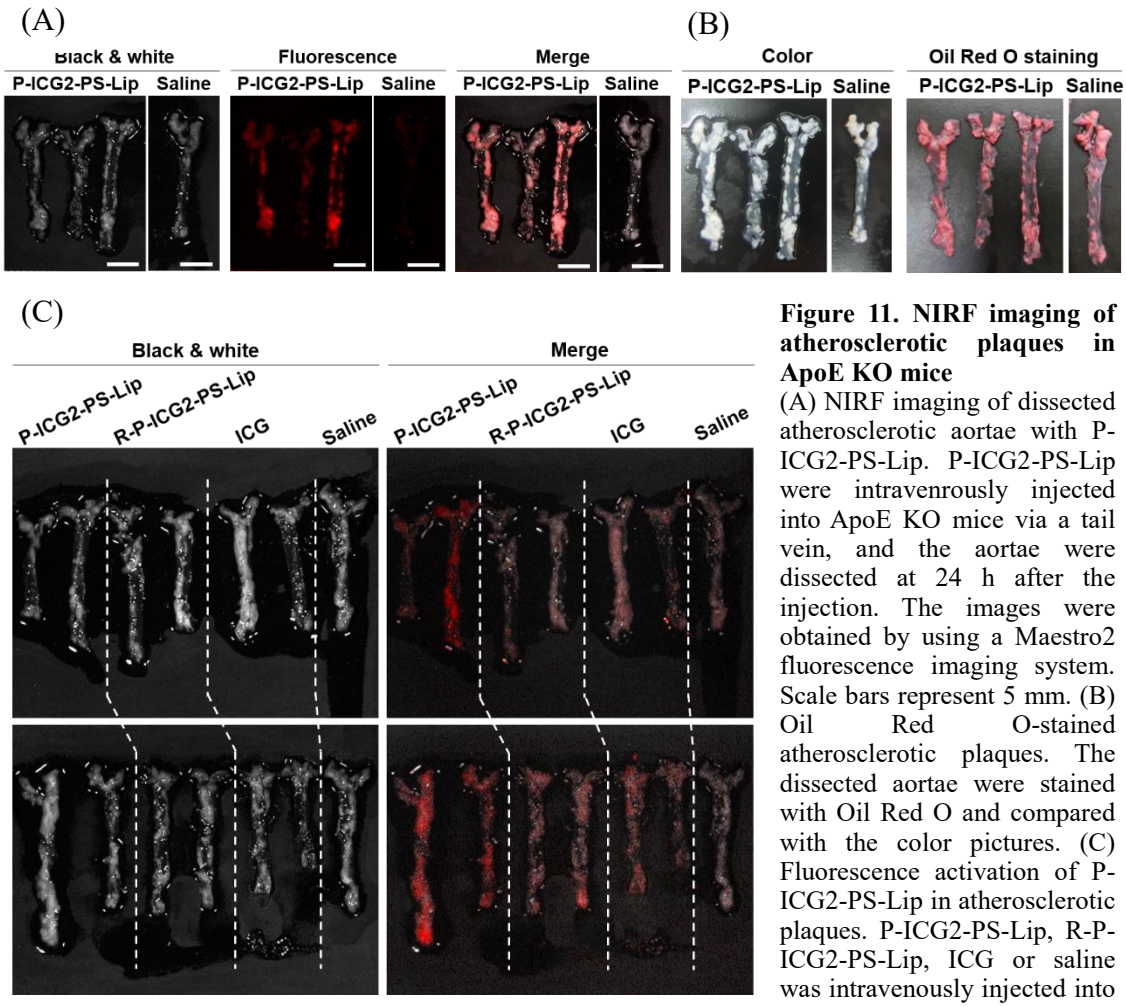

Figure 11. NIRF imaging of atherosclerotic plaques in ApoE KO mice
(A) NIRF imaging of dissected atherosclerotic aortae with P-ICG2-PS-Lip. P-ICG2-PS-Lip were intravenrously injected into ApoE KO mice via a tail vein, and the aortae were dissected at 24 h after the injection. The images were obtained by using a Maestro2 fluorescence imaging system. Scale bars represent 5 mm. (B) Oil Red O-stained atherosclerotic plaques. The dissected aortae were stained with Oil Red O and compared with the color pictures. (C) Fluorescence activation of P-ICG2-PS-Lip in atherosclerotic plaques. P-ICG2-PS-Lip, R-P-ICG2-PS-Lip, ICG or saline was intravenously injected into ApoE KO mice and after 24 h, NIRF imaging of the aortae was performed.

positive lipid-rich regions merged with those positive with the Oil Red O stain (Figure 11B), indicating that the fluorescence of P-ICG2-PS-Lip was located at the atherosclerotic plaques. Then, to demonstrate the detection specificity of P-ICG2-PS-Lip at atherosclerotic plaques, ICG, R-P-ICG2-PS-Lip, or P-ICG2-PS-Lip was injected to the ApoE KO mice and 24 hours after the injection, the isolated aortae were imaged by ICG fluorescence. The results showed that the fluorescence could be clearly detected at the plaques in the P-ICG2-PS-Lip-treated mice, in which the fluorescence level was the highest among the treated groups (Figure 11C). In addition, the fluorescence intensity at the plaques in ICG- or R-P-ICG2-PS-Lip-treated mice was similar to that in saline-treated mice, indicating their fluorescence to be at the background level (Figure 11C).

3-2-2. NIRF imaging of atherosclerotic plaques in WHHL rabbit with P-ICG2-PS-Lip

The NIRF imaging experiments were equally performed using a spontaneously atherosclerotic animal, WHHL rabbits. As the results, high-intensity ICG fluorescence signals could be detected in both the thoracic and abdominal aorta, especially, at the aortic arch where the atherosclerosis develops (Figure 12A); but the ICG signal was not detected at the aorta of P-ICG2-PS-Lip-treated normal NZW rabbit (Figure 12B). Additionally, to confirm whether fluorescence activation of P-ICG2-PS-Lip had actually occurred in macrophages in the atherosclerotic plaques, aorta sections were prepared; and immunostaining of macrophages in the plaques was carried out. Fluorescence microscopic observation showed that the ICG fluorescence co-localized with CD68-positive macrophages in the plaques (Figure 12C).

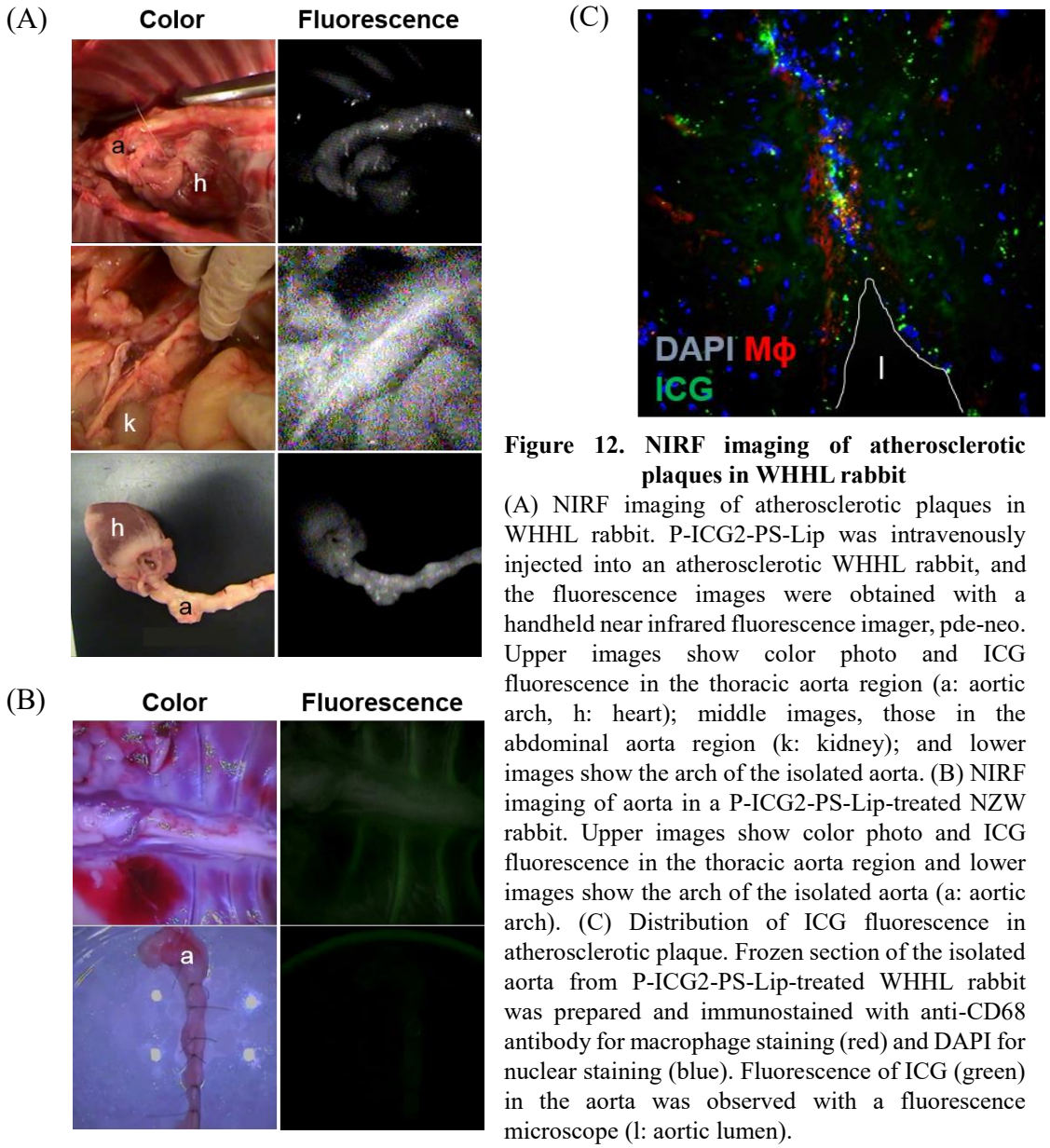

Figure 12. NIRF imaging of atherosclerotic plaques in WHHL rabbit

(A) NIRF imaging of atherosclerotic plaques in WHHL rabbit. P-ICG2-PS-Lip was intravenously injected into an atherosclerotic WHHL rabbit, and the fluorescence images were obtained with a handheld near infrared fluorescence imager, pde-neo. Upper images show color photo and ICG fluorescence in the thoracic aorta region (a: aortic arch, h: heart); middle images, those in the abdominal aorta region (k: kidney); and lower images show the arch of the isolated aorta. (B) NIRF imaging of aorta in a P-ICG2-PS-Lip-treated NZW rabbit. Upper images show color photo and ICG fluorescence in the thoracic aorta region and lower images show the arch of the isolated aorta (a: aortic arch). (C) Distribution of ICG fluorescence in atherosclerotic plaque. Frozen section of the isolated aorta from P-ICG2-PS-Lip-treated WHHL rabbit was prepared and immunostained with anti-CD68 antibody for macrophage staining (red) and DAPI for nuclear staining (blue). Fluorescence of ICG (green) in the aorta was observed with a fluorescence microscope (l: aortic lumen).

3-2-3. NIRF imaging in atherosclerotic monkeys with P-ICG2-PS-Lip

To achieve non-invasive NIRF imaging of atherosclerotic plaques in non-rodent mammalian, cynomolgus monkeys were daily fed the high-fat diet and resulted in the development of atherosclerosis. All monkeys indicated elevated levels of total and LDL cholesterols in blood and the both values have exceeded the upper limits of normal by

one month after the beginning of high-fat diet feeding and kept them during the diet feeding (Figure 13A). On the other hand, the blood concentration of HDL cholesterol kept low level after the diet feeding. Then, the carotid arteries in the monkeys were imaged by MR angiography (Figure 13B) and the tomographic analysis of the cervical region was carried out to determine the caliber of the carotid arteries and the depth from the skin surface. The obtained data of monkey fed with a high-fat diet for 22 months indicated that the caliber and depth of left carotid artery were 2.87 x 3.07 mm and 9.09 mm; and those

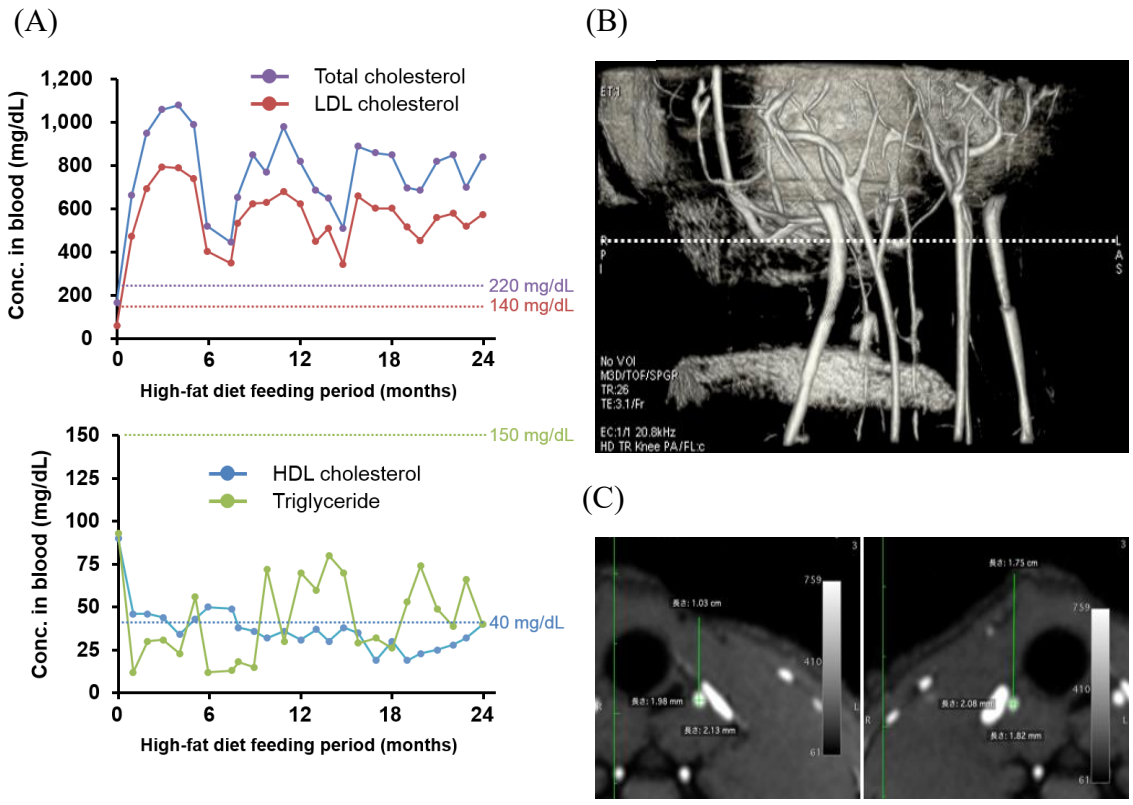

Figure 13. Preparation of atherosclerotic monkeys
(A) Biochemical values in atherosclerotic monkey. Cynomolgus monkeys were daily fed a high-fat diet in order to develop the atherosclerosis. Blood concentrations of total, LDL and HDL cholesterols and triglyceride in a representative monkey at indicated time were measured. Colored dotted lines indicated the upper limit values of normal for total, LDL cholesterols and tryglyceride and lower one for HDL cholesterol. (B) MR angiography of the carotid arteries. 3T-MRI scan was performed in the atherosclerotic monkey. White dotted line represents the scan position for non-invasive NIFR imaging of the carotid arteries. (C) Tomographic analysis of carotid arteries. The tomographic images of left (left image) and right (right image) carotid arteries were obtained and the caliber and the depth from the skin surface of the arteries were determined.

of right carotid artery were 3.14. x 3.33 mm and 9.20 mm, respectively (Figure 13C). Then the atherosclerotic monkeys were intravenously injected with ICG liposome or P-ICG2-PS-Lip and non-invasive NIRF imaging of the monkeys was performed. The result of NIRF imaging using ICG liposome indicated that the ICG dye systemically distributed throughout the body just after the injection of the liposome and high ICG fluorescence signals have been detected at whole face and cervical region (Figure 14).

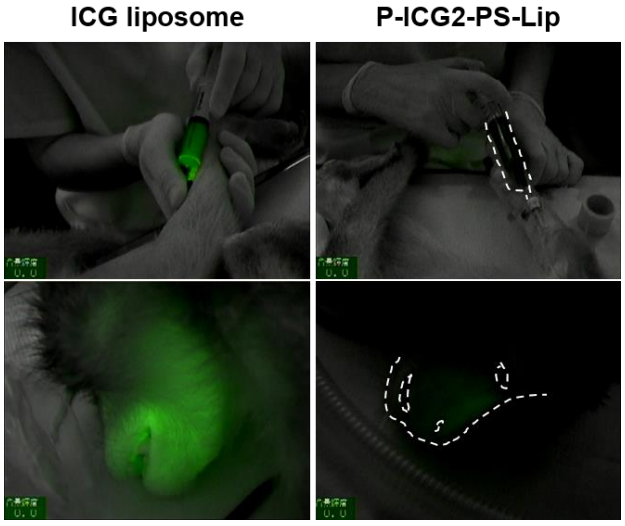

Figure 14. NIRF imaging in atherosclerotic monkeys

ICG liposome (approximately 780 μg as an ICG dose) (left images) or P-ICG2-PS-Lip (approximately 1.24 mg as a Peptide-ICG2 dose) (right images) was intravenously injected to atherosclerotic monkeys and non-invasive NIRF imaging with pde-neo was carried out. Upper images represent the fluorescence of each sample before the injection. Lower images represent the fluorescence around monkey head just after the injection. White dotted lines show the positions of a syringe filled with P-ICG2-PS-Lip (upper) and monkey's face (lower), respectively.

On the other hands, the result of NIRF imaging using P-ICG2-PS-Lip indicated that non-specific fluorescence signals at the face and cervical regions were obviously suppressed and the background signal was quite low (Figure 14).

Because non-specific ICG fluorescence at the cervical region of ICG liposome-treated monkey remained high level 6 h after the injection, non-invasive NIRF imaging of the atherosclerotic plaques in the monkey using ICG liposome was given up and the carotid artery was exposed by surgically incising the skin and fascia. Then, the NIRF imaging with the pde-neo alone (Method 1, Figure 15A) was again carried out. As the result, the ICG fluorescence signal at the carotid artery was quite low and it was difficult to identify the atherosclerotic plaques, while the carotid artery was exteriorized. On the

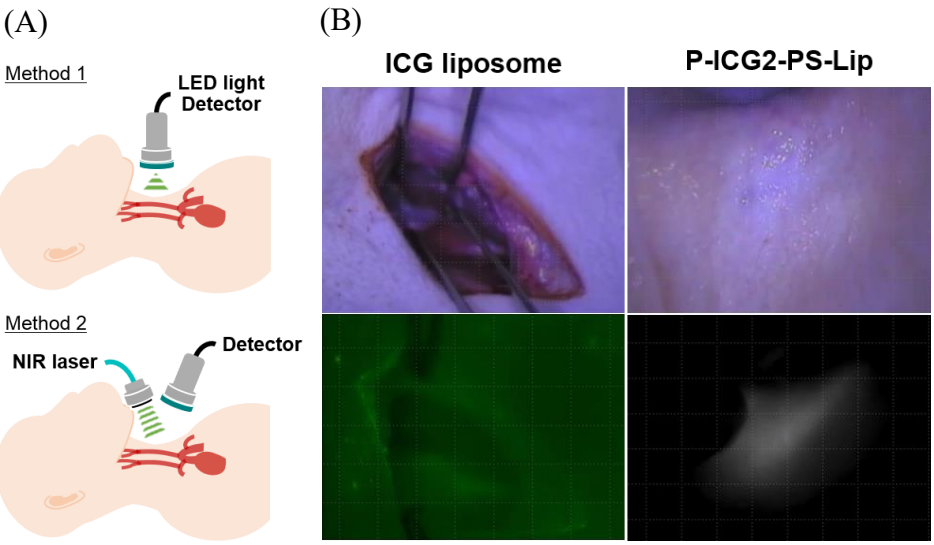

Figure 15. NIRF imaging at cervical region of atherosclerotic monkeys
(A) Illustrations of NIRF imaging methods. Method 1 is an imaging procedure using a pde-neo alone that equipped with both LED light for excitation and detector camera unit for ICG fluorescence detection. Method 2 is another imaging procedure using both a high-power NIR laser for excitation and the pde-neo as a detector, which enables to enhance the detection sensitivity of ICG fluorescence. (B) NIRF imaging of atherosclerotic plaques. ICG liposome (left images) or P-ICG2-PS-Lip (right images) was intravenously injected to the cynomolgus monkeys and allowed to circulate for 6 h. The cervical region of ICG liposome-treated monkey was incised and the carotid artery was exposed. The fluorescence images of ICG liposome-treated monkey were obtained by Method 1. On the other hand, non-invasive NIRF imaging was performed in P-ICG2-PS-Lip-treated monkey. The fluorescence images were obtained by Method 2.

other hand, to improve the detection sensitivity of ICG fluorescence by the pde-neo, the other detection system, in which the ICG fluorescence was scanned by the pde-neo following excitation of the ICG dye with a high-power laser (Method 2, Figure 15A), was adopted, and then non-invasive NIRF imaging of the atherosclerotic plaques in the atherosclerotic monkey injected with P-ICG2-PS-Lip was performed. As the result of the fluorescence imaging at the cervical region, a linear fluorescence signal just like the atherosclerotic artery could be found without surgical operation of the monkey (Figure 15B). Moreover, to confirm what the fluorescence is derived from, the aorta and carotid arteries were dissected from the monkey and *ex vivo* NIRF images of them were obtained with the pde-neo. The results demonstrated the ICG fluorescence were clearly found at

not only the aorta including aortic arch, but also the carotid arteries, where develops the atherosclerotic plaques (Figure 16B).

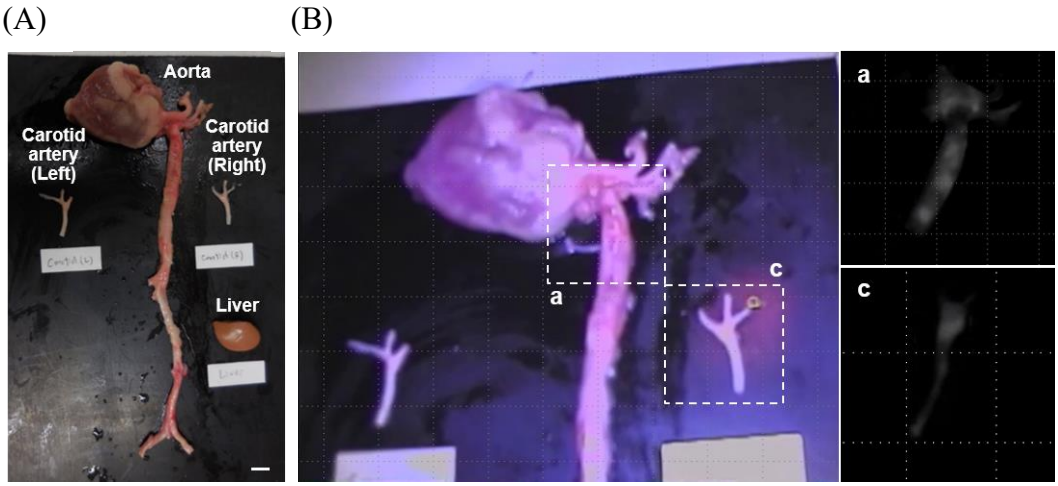

Figure 16. *Ex vivo* NIRF imaging of atherosclerotic plaques in monkeys
(A) Photo of the dissected atherosclerotic lesions. Aorta including heart, carotid arteries, and liver were dissected from the P-ICG2-PS-Lip-treated monkey (approximately 290 μg as a Peptide-ICG2 dose). Scale bar represents 10 mm. (B) *Ex vivo* NIRF imaging of the aorta and carotid arteries. The color (left image) and fluorescence images (right images) were obtained using the pde-neo. Field of view of each fluorescence image was shown as white dotted boxes (a: aorta, c: right carotid artery) in the left image.

3-2-4. PA imaging in ApoE KO mouse with P-ICG2-PS-Lip

Although the fluorescence signals at carotid artery of P-ICG2-PS-Lip-treated monkey could be detected by NIRF imaging, the image was not clear and it was difficult to confirm the location of the atherosclerotic plaques. Therefore, I tried to apply other optical imaging, PA imaging to the detection of the atherosclerotic plaques, since the PA imaging can overcome the weakness of fluorescence imaging such as decrease of detection signal in a deep area. P-ICG2-PS-Lip was intravenously injected to the ApoE KO mice and after 24 h, PA imaging was performed by using the MSOT system. As the results, PA signal of ICG was successfully obtained and detected at the mouse chest in sequential tomographic images. PA signal of HbO_2 that represent the location of aorta was

similarly detected in the chest and merged with that of ICG (Figure 17).

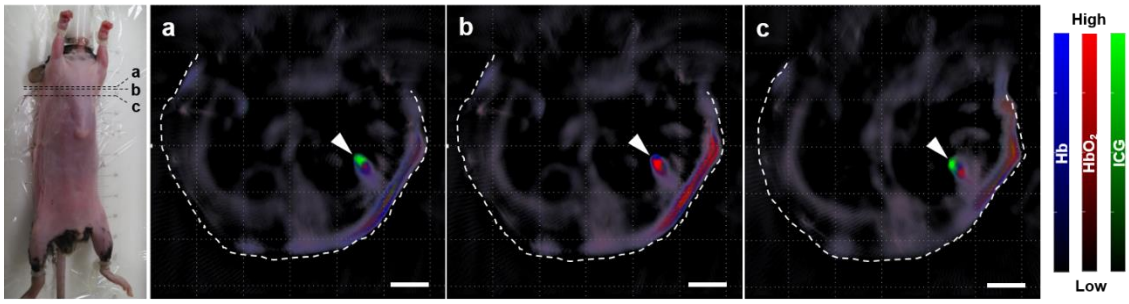

Figure 17. PA imaging of atherosclerotic plaques in ApoE KO mice
Non-invasive PA imaging was performed with ApoE KO mouse. The PA images of hemoglobin (Hb, blue), oxyhemoglobin (HbO_2, red) and ICG (green) were obtained at 24 h after intravenous injection of P-ICG2-PS-Lip. Positions of vertical tomographic images (a-c) were shown in left image. White dotted line represents the mouse body outline. Arrowhead indicates the location of the aorta. Scale bars represent 3 mm.

3-2-5. PA imaging in atherosclerotic monkey with P-ICG2-PS-Lip

Finally, PA imaging was applied to the detection of atherosclerotic plaques in atherosclerotic monkey and the non-invasive PA scan was performed by attaching the handheld detector with the cervical skin of the P-ICG2-PS-Lip-treated monkey to detect the atherosclerotic plaques at the carotid artery (Figure 18A). The location of the carotid artery was determined by the ultrasound-like morphological image which was obtained from the PA signal at the reference wavelength of near infrared region and the carotid artery pulsation could be observed during the real-time imaging. The results indicated that PA signals of ICG could be clearly observed at the carotid artery. (Figure 18B). Then the aorta and the carotid arteries were dissected and *ex vivo* PA imaging of them was carried out. As the result, PA signals of ICG could be detected at the carotid arteries and was merged with the location of atherosclerotic plaques (Figure 19A). Similarly, the PA signals of ICG were observed at atherosclerotic plaques in the aorta including aortic arch

(Figure 19B).

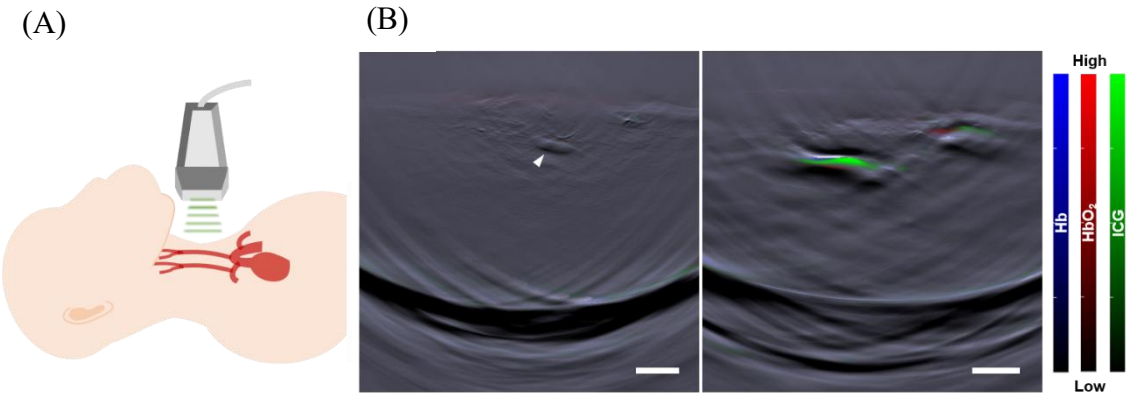

Figure 18. PA imaging of atherosclerotic plaques in atherosclerotic monkeys
(A) Illustration of PA imaging for detection of atherosclerotic plaques. To detect the PA signals at carotid artery, a handheld MSOT detector was used and attached to the cervical region of the monkey. (B) PA imaging of atherosclerotic plaques. P-ICG2-PS-Lip was intravenously injected to the atherosclerotic monkey and 3 h after the injection, PA imaging at the cervical region was non-invasively performed in real time under isoflurane anesthesia. PA signals of Hb (blue), HbO_2 (red), and ICG (green) were separated according to the information of each standard PA spectrum and shown in the tomographic image. Left image represents morphological image which was obtained from the PA signal at the reference wavelength of near infrared region and arrowhead was shown at a location of carotid artery. Right image represents merged morphological and PA image. Scale bars represent 5 mm.

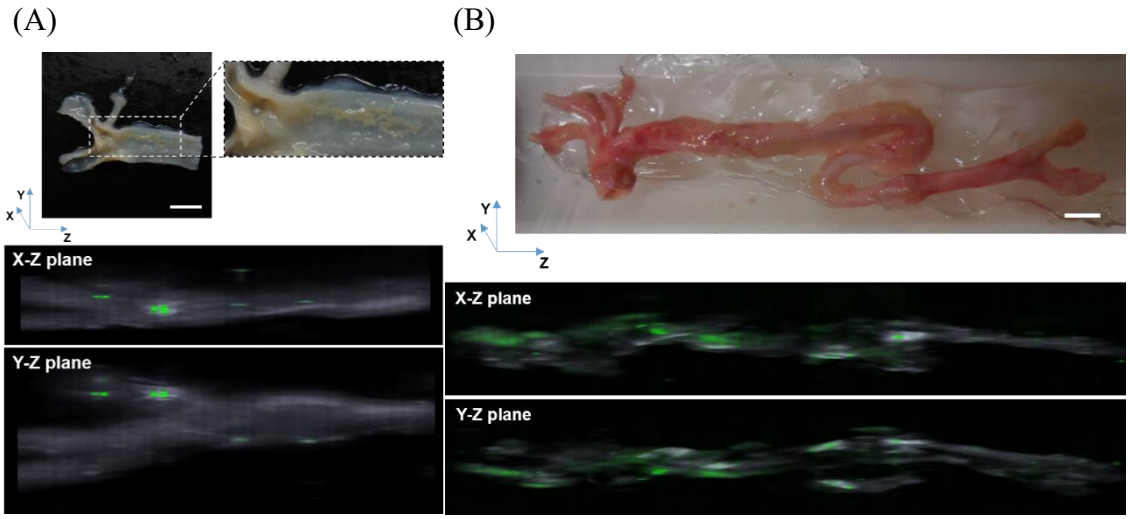

Figure 19. *Ex vivo* PA imaging of atherosclerotic plaques in atherosclerotic monkeys
(A) PA imaging of carotid artery isolated from atherosclerotic monkey. The carotid artery was dissected from P-ICG2-PS-Lip-treated monkey and cut open to expose the intima. Photo of the open carotid artery was shown (upper left image) and the atherosclerotic lesions were magnified (upper right image).The PA images were shown as 2D images (X-Z and Y-Z planes), which were obtained according to xyz-axis in upper image. Scale bar represents 5 mm. (B) PA imaging of atherosclerotic aorta. The aorta including aortic arch was isolated from the P-ICG2-PS-Lip-treated atherosclerotic monkey (upper image). The PA images were shown as 2D X-Z plane (middle image) and Y-Z plane (lower image), which were obtained according to xyz-axis in upper image. Scale bar represents 10 mm.

3-3. Discussion

In this chapter, I evaluated the usefulness of P-ICG2-PS-Lip for optical imaging of embolism-vulnerable atherosclerotic plaques *in vivo*. Since the ApoE KO mouse and WHHL rabbit are widely used as animal models of atherosclerosis [61-64] and display lipid-rich plaques at arterial vessel walls, especially in the thoracic arch of the aorta, I first used these models for NIRF imaging of the atherosclerotic plaques with P-ICG2-PS-Lip. NIRF imaging after the systemic injection of P-ICG2-PS-Lip to the atherosclerotic animals resulted that strong fluorescence signals could be observed at the isolated aortae of both animals and the detection was dependent on the cathepsin B activity. These findings suggest that both active delivery of the fluorescence dye to atherosclerotic macrophages and the fluorescence activation at the atherosclerotic plaques

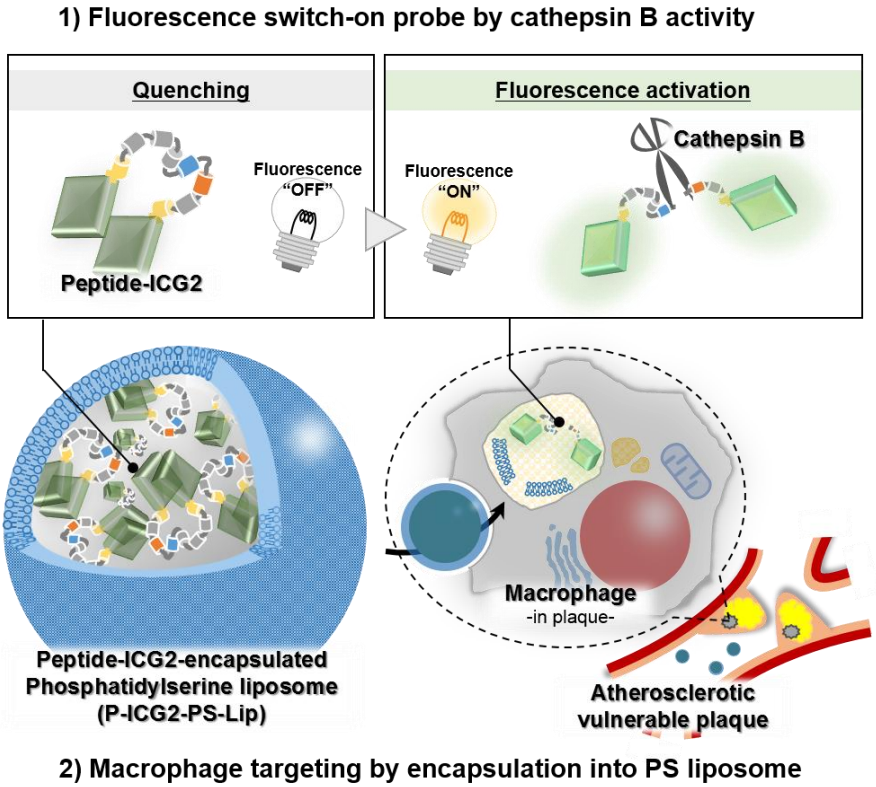

Scheme 6. Strategy of atherosclerotic vulnerable plaque imaging with P-ICG2-PS-Lip

are important to obtain the clear fluorescence images of atherosclerotic lesions and I proposed a molecular imaging strategy of atherosclerosis diagnosis using P-ICG2-PS-Lip, which was illustrated in Scheme 7. P-ICG2-PS-Lip have 2 functional aspects for specific detection of embolism-vulnerable atherosclerotic plaques: 1) Fluorescence switch-on probe of Peptide-ICG2 triggered by cathepsin B enzymatic activity; and 2) macrophage-targeting DDS by PS liposome. That is, P-ICG2-PS-Lip is delivered to macrophages in embolism-vulnerable atherosclerotic plaques by PS-mediated targeting; and the fluorescence of Peptide-ICG2 is enzymatically activated at lysosomes in the macrophage cells, resulting in fluorescence signal generation at the atherosclerotic plaques. Since embolism-vulnerability of atherosclerotic plaques is determined by the existence of infiltrating macrophages, P-ICG2-PS-Lip would be a potential imaging agent for diagnosis of atherosclerosis and potential future embolism.

To demonstrate the possibility of the P-ICG2-PS-Lip for the application to non-invasive diagnosis of atherosclerosis, atherosclerotic monkey was prepared. As mentioned in the introduction, the carotid ultrasound imaging is clinically used for diagnosis of atherosclerosis, because the carotid arteries are common sites at which atherosclerotic plaques are prone to be formed and its diagnostic information accurately correlates with the development of systemic atherosclerosis. In addition, the cervical structure of monkey is quite similar to that of human and the atherosclerotic plaque formation is observed at the carotid arteries following daily high-fat diet feeding to the monkey. These evidences strongly promise the importance of the utility evaluation of P-ICG2-PS-Lip using atherosclerotic monkey before clinical application. As the results of NIRF imaging of the monkey cervical region, P-ICG2-PS-Lip suppressed non-specific fluorescence signals at the cervical region compared with ICG liposome, suggesting that

the fluorescence quenching of P-ICG2-PS-Lip works well in the monkey. However, clear fluorescence images of the atherosclerotic plaques at the carotid artery could not be obtained in the experiment. I thought the reason was due to the detection limit of NIRF signals at deep area brought by light scatter and absorption, that is known to be up to about 1 cm in depth. In fact, the distance of carotid arteries from skin surface of the monkey obtained from MR angiography was approximately 1 cm. Monkeys generally have thick cervical muscles compared with humans due to their quadrupedalism and I therefore thought it was difficult to detect the fluorescence signals at the carotid artery in the monkey. Since the carotid arteries of human are contrastingly located in the near distance from the neck skin, I believe my NIRF imaging strategy with P-ICG2-PS-Lip could be applicable to the detection of carotid atherosclerotic plaques in human.

Photoacoustic imaging is an optical imaging modality based on laser-generated ultrasounds that enable to detect the optical signals in a deep tissue and now attracting a great deal of attention. Indeed, photoacoustic imaging has been recently applied in both basic and clinical studies on disease diagnosis, especially cancer diagnosis [65-67]. ICG is well used commonly as a NIRF dye, whereas it can also be suitable as a photoacoustic probe [68,69]: Fluorescence quantum efficiency of ICG is quite low (about 2% in water) and absorbed light energy would be largely transferred to heat energy. Actually, there are some reports about the development of ICG-conjugated probes for photoacoustic imaging and the detection of disease sites in deep tissues has been successful by taking advantage of the photoacoustic characteristics [70]. Therefore, I assumed that P-ICG2-PS-Lip is also applicable to photoacoustic imaging, because P-ICG2-PS-Lip is activated in atherosclerotic plaques and the optical signal of ICG subsequently becomes detectable. As the result of photoacoustic imaging in P-ICG2-PS-Lip-treated ApoE KO mice,

photoacoustic signals of ICG was specifically detected at the thoracic aorta of the mice. On the basis of the findings of photoacoustic imaging with P-ICG2-PS-Lip in ApoE KO mice, I finally attempted to image atherosclerotic plaques at the carotid artery of atherosclerotic monkey non-invasively. Consequently, I succeeded to obtain clear images of the carotid atherosclerotic lesions. Since there have been little reports about non-invasive atherosclerotic plaque detection in atherosclerotic monkey by using easy-to-use optical imaging, my findings in this study could be of significance to atherosclerosis diagnosis. Recently, nanoparticle-based delivery systems have become applicable to atherosclerosis imaging [71-74]. Additionally, the development of activatable photoacoustic probes has been reported [75,76]. It has the possibility that P-ICG2-PS-Lip similarly worked as an activatable photoacoustic probe sensed by cathepsin B. These molecular imaging methodologies using unique optical imaging probes would be useful to understand the biology of atherosclerotic plaques and monitor the clinical condition of atherosclerosis. I am convinced that the present study using P-ICG2-PS-Lip can achieve specific imaging of the atherosclerotic lesions by a combination system of the enzyme-specific optical switch-on probe with macrophage-targetable liposome delivery.

Conclusion

In this study, I developed a novel optical imaging system, P-ICG2-PS-Lip for a detection of atherosclerotic vulnerable plaques: Peptide-ICG2, a fluorescence switch-on probe, worked for specific detection of either the ICG fluorescence signal or the ICG photoacoustic one in macrophages; and PS liposome, an active targeting nanocarrier, could deliver the Peptide-ICG2 to macrophages that had infiltrated into atherosclerotic plaques. Using this approach, I demonstrated the successful detection of atherosclerotic plaques in atherosclerotic model animals. Whereas fluorescence imaging detects only signals from tissues near the surface of the body but not those present in deeper parts, NIRF and photoacoustic imaging systems developed in this research may overcome this limitation, allowing for detection of deep parts of the atherosclerotic lesion, although further studies should be conducted. I believe that the present study becomes a platform for the detection of atherosclerotic plaques and may be applicable to the diagnosis of atherosclerosis in the future.

Acknowledgments

This dissertation is a report that was carried out at Department of Medical Biochemistry, University of Shizuoka and some experiments were done at Laboratory of Molecular Imaging, Hamamatsu University School of Medicine, to which I belong as a research student.

First, I would like to express my gratitude to my supervisor, Professor Naoto Oku and Professor Tomohiro Asai, University of Shizuoka and Professor Yasuhiro Magata, Hamamatsu University School of Medicine for providing me this precious study opportunity as a Ph.D student in his laboratory and supporting my school life. I am deeply grateful to my supervisor, Dr. Kousuke Shimizu, Hamamatsu University School of Medicine for their elaborated guidance, considerable encouragement and invaluable discussion that make my research of great achievement and also thank co-researcher, Professor Mikako Ogawa, Hokkaido University for supporting everything of this study. I appreciate everyone at the Department of Medical Biochemistry, University of Shizuoka and Laboratory of Molecular Imaging, Hamamatsu University School of Medicine for my encouragements.

I then would like to thank all collaborative researchers who have supported this work. I greatly acknowledge Dr. Kazuya Hokamura, Hamamatsu University School of Medicine for supporting the experiments using monkey models, Dr. Takahiro Natsume, Hamamatsu Pharma Research, Inc. (Shizuoka, Japan) for performing MRI and X-ray CT scan, Mr. Mitsuharu Miwa and Mr. Kazumasa Hirawake, Hamamatsu Photonics K.K. for engineering near-infrared laser and filter and Mr. Shigeaki Watanabe and Ms. Hitomi Miyabara, Summit Phaceutical International Co. (Tokyo, Japan) for analyzing by PA

imaging.

I greatly appreciate Prof. Tatuya Morimoto, Prof. Satomi Onoue and Prof. Kenichiro Todoroki for helpful discussion and suggestion. I am very grateful to Mr. Keisuke Ikemoto, Mr. Yoshihito Takeuchi, Mr. Kazuma Otuka, Mr. Kazuki Agata, Mr. Shohei Takasugi and Mr. Tomoya Mori for their valuable cooperation in my experiments.

Finally, I would like to extend my indebtedness to my family, Saki, Mitsuaki, Makiko, Ayaka, Nana for their endless love, understanding, support, encouragement and sacrifice throughout my study.

References

[1] A.J. Lusis, Atherosclerosis, Nature 407 (2000) 233-241.

[2] Top 10 causes of death in 2016 according to Global Health Observatory (GHO) data on World Health Organization (WHO). Available from URL: http://www.who.int/gho/mortality_burden_disease/causes_death/top_10/en/

[3] R. Virmani, A.P. Burke, F.D. Kolodgie, A. Farb, Vulnerable plaque: the pathology of unstable coronary lesions, J. Interv. Cardiol. 15 (2002) 439-446.

[4] J.F. Bentzon, F. Otsuka, R. Virmani, E. Falk, Mechanisms of plaque formation and rupture, Circ. Res. 114 (2014) 1852-1866.

[5] J.E. Muller, G.S. Abela, R.W. Nesto, G.H. Tofler, Triggers, acute risk factors and vulnerable plaques: the lexicon of a new frontier, J. Am. Coll. Cardiol. 23 (1994) 809-813.

[6] P. Libby, Y.J. Geng, M. Aikawa, U. Schoenbeck, F. Mach, S.K. Clinton, G.K. Sukhova, R.T. Lee, Macrophages and atherosclerotic plaque stability, Curr. Opin. Lipidol. 7 (1996) 330-335.

[7] P. Libby, Coronary artery injury and the biology of atherosclerosis: inflammation, thrombosis, and stabilization, Am. J. Cardiol. 86 (2000) 3J-9J.

[8] Z. Varasteh, F. Hyafil, N. Anizan, D. Diallo, R. Aid-Launais, S. Mohanta, Y. Li, M. Braeuer, K. Steiger, J. Vigne, Z. Qin, S.G. Nekolla, J.E. Fabre, Y. Döring, D. Le Guludec, A. Habenicht, D.R. Vera, M. Schwaiger, Targeting mannose receptor expression on macrophages in atherosclerotic plaques of apolipoprotein E-knockout mice using ^{111}In-tilmanocept, EJNMMI Res. 7 (2017) 40.

[9] N. MacRitchie, G. Grassia, J. Noonan, P. Garside, D. Graham, P. Maffia, Molecular imaging of atherosclerosis: spotlight on Raman spectroscopy and surface-enhanced Raman scattering, Heart 104 (2018) 460-467.

[10] T. Noguchi, T. Kawasaki, A. Tanaka, S. Yasuda, Y. Goto, M. Ishihara, K. Nishimura, Y. Miyamoto, K. Node, N. Koga, High-intensity signals in coronary plaques on noncontrast T1-weighted magnetic resonance imaging as a novel determinant of coronary events, J. Am. Coll. Cardiol. 63 (2014) 989-999.

[11] K. Matsumoto, S. Ehara, T. Hasegawa, M. Sakaguchi, K. Otsuka, J. Yoshikawa, K. Shimada, Localization of coronary high-intensity signals on T1-weighted MR imaging: relation to plaque morphology and clinical severity of angina pectoris, JACC Cardiovasc. Imaging 8 (2015) 1143-1152.

[12] S. Ehara, K. Matsumoto, K. Shimada, The clinical value of high-intensity signals on the coronary atherosclerotic plaques: noncontrast T1-weighted magnetic

resonanceimaging, Int. J. Mol. Sci. 17 (2016) E1187.

[13] J.H. Rudd, J. Narula, H.W. Strauss, R. Virmani, J. Machac, M. Klimas, N. Tahara, V. Fuster, E.A. Warburton, Z.A. Fayad, A.A. Tawakol, Imaging atherosclerotic plaque inflammation by fluorodeoxyglucose with positron emission tomography: ready for prime time? J. Am. Coll. Cardiol. 55 (2010) 2527-2535.

[14] A.L. Figueroa, A. Abdelbaky, Q.A. Truong, E. Corsini, M.H. MacNabb, Z.R. Lavender, M.A. Lawler, S.K. Grinspoon, T.J. Brady, K. Nasir, U. Hoffmann, A. Tawakol, Measurement of arterial activity on routine FDG PET/CT images improves prediction of risk of future CV events, JACC Cardiovasc. Imaging 6 (2013) 1250-1259.

[15] M.R. Dweck, M.W. Chow, NV. Joshi, M.C. Williams, C. Jones, A.M. Fletcher, H. Richardson, A. White, G. McKillop, E.J. van Beek, N.A. Boon, J.H. Rudd, D.E. Newby, Coronary arterial ^{18}F-sodium fluoride uptake: a novel marker of plaque biology, J. Am. Coll. Cardiol. 59 (2012) 1539-1548.

[16] N.V. Joshi, A.T. Vesey, M.C. Williams, A.S. Shah, P.A. Calvert, F.H. Craighead, S.E. Yeoh, W. Wallace, D. Salter, A.M. Fletcher, E.J. van Beek, A.D. Flapan, N.G. Uren, M.W. Behan, N.L. Cruden, N.L. Mills, K.A. Fox, J.H. Rudd, M.R. Dweck, D.E. Newby, ^{18}F-fluoride positron emission tomography for identification of ruptured and high-risk coronary atherosclerotic plaques: a prospective clinical trial, Lancet 383 (2014) 705-713.

[17] M. Ogawa, S. Ishino, T. Mukai, D. Asano, N. Teramoto, H. Watabe, N. Kudomi, M. Shiomi, Y. Magata, H. Iida, H. Saji, ^{18}F-FDG accumulation in atherosclerotic plaques: immunohistochemical and PET imaging study, J. Nucl. Med. 45 (2004) 1245-1250.

[18] M. Ogawa, S. Nakamura, Y. Saito, M. Kosugi, Y. Magata, What can be seen by ^{18}F-FDG PET in atherosclerosis imaging? The effect of foam cell formation on ^{18}F-FDG uptake to macrophages in vitro, J. Nucl. Med. 53 (2012) 55-58.

[19] M. Ogawa, Y. Magata, T. Kato, K. Hatano, S. Ishino, T. Mukai, M. Shiomi, K. Ito, H. Saji, Application of ^{18}F-FDG PET for monitoring the therapeutic effect of antiinflammatory drugs on stabilization of vulnerable atherosclerotic plaques, J. Nucl. Med. 47 (2006) 1845-1850.

[20] M. Ogawa, I.O. Umeda, M. Kosugi, A. Kawai, Y. Hamaya, M. Takashima, H. Yin, T. Kudoh, M. Seno, Y. Magata, Development of ^{111}In-labeled liposomes for vulnerable atherosclerotic plaque imaging, J. Nucl. Med. 55 (2014) 115-120.

[21] Y. Urano, D. Asanuma, Y. Hama, Y. Koyama, T. Barrett, M. Kamiya, T. Nagano, T. Watanabe, A. Hasegawa, P.L. Choyke, H. Kobayashi, Selective molecular imaging

of viable cancer cells with pH-activatable fluorescence probes, Nat. Med. 15 (2009) 104–109.

[22] H. Kobayashi, M. Ogawa, R. Alford, P.L. Choyke, Y. Urano, New strategies for fluorescent probe design in medical diagnostic imaging, Chem. Rev. 110 (2010) 2620–2640.

[23] S. Jormsjö, D.M. Wuttge, A. Sirsjö, C. Whatling, A. Hamsten, S. Stemme, P. Eriksson, Differential expression of cysteine and aspartic proteases during progression of atherosclerosis in apolipoprotein E-deficient mice, Am. J. Pathol. 161 (2002) 939-945.

[24] I. Abd-Elrahman, K. Meir, H. Kosuge, Y. Ben-Nun, T. Weiss Sadan, C. Rubinstein, Y. Samet, M.V. McConnell, G. Blum, Characterizing cathepsin activity and macrophage subtypes in excised human carotid plaques, Stroke 47 (2016) 1101-1108.

[25] C.F. Zhao, D.M. Herrington, The function of cathepsins B, D, and X in atherosclerosis, Am. J. Cardiovasc. Dis. 6 (2016) 163-170.

[26] T. Weiss-Sadan, I. Gotsman, G. Blum, Cysteine proteases in atherosclerosis, FEBS J. 284 (2017) 1455-1472.

[27] D.E. Kim, J.Y. Kim, D. Schellingerhout, S.M. Shon, S.W. Jeong, E.J. Kim, W.K. Kim, Molecular imaging of cathepsin B proteolytic enzyme activity reflects the inflammatory component of atherosclerotic pathology and can quantitatively demonstrate the antiatherosclerotic therapeutic effects of atorvastatin and glucosamine, Mol. Imaging 8 (2009) 291-301.

[28] M. Nahrendorf, P. Waterman, G. Thurber, K. Groves, M. Rajopadhye, P. Panizzi, B. Marinelli, E. Aikawa, M.J. Pittet, F.K. Swirski, R. Weissleder, Hybrid in vivo FMT-CT imaging of protease activity in atherosclerosis with customized nanosensors, Arterioscler. Thromb. Vasc. Biol. 29 (2009) 1444-1451.

[29] I. Abd-Elrahman, H. Kosuge, T. Wises Sadan, Y. Ben-Nun, K. Meir, C. Rubinstein, M. Bogyo, M.V. McConnell, G. Blum, Cathepsin activity-based probes and inhibitor for preclinical atherosclerosis imaging and macrophage depletion, PLoS One 11 (2016) e0160522.

[30] K. Segawa, S. Nagata, An apoptotic 'Eat me' signal: phosphatidylserine exposure, Trends Cell Biol. 25 (2015) 639-650.

[31] D. Asanuma, Y. Takaoka, S. Namiki, K. Takikawa, M. Kamiya, T. Nagano, Y. Urano, K. Hirose, Acidic-pH-activatable fluorescence probes for visualizing exocytosis dynamics, Angew. Chem. Int. Ed. Engl. 53 (2014) 6085-6089.

[32] D. Asanuma, M. Sakabe, M. Kamiya, K. Yamamoto, J. Hiratake, M. Ogawa, N. Kosaka, P.L. Choyke, T. Nagano, H. Kobayashi, Y. Urano, Sensitive β-galactosidase-

targeting fluorescence probe for visualizing small peritoneal metastatic tumours in vivo, Nat. Commun. 6 (2015) 6463.

[33] K. Setsukinai, Y. Urano, K. Kakinuma, H.J. Majima, T. Nagano, Development of novel fluorescence probes that can reliably detect reactive oxygen species and distinguish specific species, J. Biol. Chem. 278 (2003) 3170-3175.

[34] T. Komatsu, Y. Urano, Evaluation of enzymatic activities in living systems with small-molecular fluorescent substrate probes, Anal. Sci. 31(2015) 257-265.

[35] Bioconjugate Techniques 3rd edition (2013), Greg T. Hermanson

[36] F. Bergström, I. Mikhalyov, P. Hägglöf, R. Wortmann, T. Ny, L.B. Johansson, Dimers of dipyrrometheneboron difluoride (BODIPY) with light spectroscopic applications in chemistry and biology, J. Am. Chem. Soc. 124 (2002) 196-204.

[37] D. Setiawan, A. Kazaryan, M.A. Martoprawiro, M. Filatov, A first principles study of fluorescence quenching in rhodamine B dimers: how can quenching occur in dimeric species? Phys. Chem. Chem. Phys. 12 (2010) 11238-11244.

[38] M. Ogawa, N. Kosaka, P.L. Choyke, H. Kobayashi, H-type dimer formation of fluorophores: a mechanism for activatable, in vivo optical molecular imaging, ACS Chem. Biol. 4 (2009) 535-546.

[39] H.N. Hodis, J.K. Amartey, D.W. Crawford, E. Wickham, R.C. Sharma, D.H. Blankenhorn, Relationship of arterial wall uptake of radiolabeled liposomes to the presence of monocyte/macrophage cells in the hypertensive and atherosclerotic arterial wall, Atherosclerosis 87 (1991) 109-17.

[40] R. Hanayama, M. Tanaka, K. Miwa, A. Shinohara, A. Iwamatsu, S. Nagata, Identification of a factor that links apoptotic cells to phagocytes, Nature 417 (2002) 182-187.

[41] G. Lemke, Biology of the TAM receptors, Cold Spring Harb. Perspect. Biol. 5 (2013) a009076.

[42] M. Miyanishi, K. Tada, M. Koike, Y. Uchiyama, T. Kitamura, S. Nagata, Identification of Tim4 as a phosphatidylserine receptor, Nature 450 (2007) 435-439.

[43] S.J. Gardai, D.L. Bratton, C.A. Ogden, P.M. Henson, Recognition ligands on apoptotic cells: a perspective, J. Leukoc. Biol. 79 (2006) 896-903.

[44] C. Peter, S. Wesselborg, K. Lauber, Molecular suicide notes: last call from apoptosing cells, J. Mol. Cell Biol. 2 (2010) 78-80.

[45] K.S. Ravichandran, Beginnings of a good apoptotic meal: the find-me and eat-me signaling pathways, Immunity 35 (2011) 445-455.

[46] J.S. Lee, S.Y. Hwang, E.K. Lee, Imaging-based analysis of liposome internalization to macrophage cells: Effects of liposome size and surface modification with PEG

moiety, Colloid. Surf. B. 136 (2015) 786-90.
[47] C. Kelly, C. Jefferies, S.A. Cryan, Targeted liposomal drug delivery to monocytes and macrophages, J. Drug Deliv. 2011 (2011) 727241.
[48] S. Chono, Y. Tauchi, K. Morimoto, Pharmacokinetic analysis of the uptake of liposomes by macrophages and foam cells in vitro and their distribution to atherosclerotic lesions in mice, Drug Metab. Pharmacokinet. 21 (2006) 37-44.
[49] P. Libby, P.M. Ridker, GK. Hansson, Progress and challenges in translating the biology of atherosclerosis, Nature 473 (2011) 317-325.
[50] J.P. Mauldin, S. Srinivasan, A. Mulya, A. Gebre, J.S. Parks, A. Daugherty, C.C. Hedrick, Reduction in ABCG1 in type 2 diabetic mice increases macrophage foam cell formation, J. Biol. Chem. 281 (2006) 21216-21224.
[51] A.V. Andriyanov, E. Portnoy, E. Koren, S. Inesa, S. Eyal, S.N. Goldberg, Y. Barenholz, Therapeutic efficacy of combined PEGylated liposomal doxorubicin and radiofrequency ablation: Comparing single and combined therapy in young and old mice, J. Control. Release 257 (2017) 2-9.
[52] T. Lajunen, R. Nurmi, D. Wilbie, T. Ruoslahti, N.G. Johansson, O. Korhonen, T. Rog, A. Bunker, M. Ruponen, A. Urtti, The effect of light sensitizer localization on the stability of indocyanine green liposomes, J. Control. Release 284 (2018) 213-223.
[53] D. Sheng, T. Liu, L. Deng, L. Zhang, X. Li, J. Xu, L. Hao, P. Li, H. Ran, H. Chen, Z. Wang, Perfluorooctyl bromide & indocyanine green co-loaded nanoliposomes for enhanced multimodal imaging-guided phototherapy, Biomaterials 165 (2018) 1-13.
[54] S. Clerc, Y. Barenholz, Loading of amphipathic weak acids into liposomes in response to transmembrane calcium acetate gradients, Biochim. Biophys. Acta. 1240 (1995) 257-265.
[55] J. Qin, D. Chen, W. Lu, H. Xu, C. Yan, H. Hu, B. Chen, M. Qiao, X. Zhao, Preparation, characterization, and evaluation of liposomal ferulic acid in vitro and in vivo, Drug Dev. Ind. Pharm. 34 (2008) 602-608.
[56] K.J. Baker, Binding of sulfobromophthalein (BSP) sodium and indocyanine green (ICG) by plasma alpha-1 lipoproteins, Proc. Soc. Exp. Biol. Med. 122 (1966) 957-963.
[57] Y. Barenholz, Doxil®--the first FDA-approved nano-drug: lessons learned, J. Control. Release. 160 (2012) 117-134.
[58] K.D. Lee, K. Hong, D. Papahadjopoulos, Recognition of liposomes by cells: in vitro binding and endocytosis mediated by specific lipid headgroups and surface charge density, Biochim. Biophys. Acta. 1103 (1992) 185-197.
[59] V. Turk, B. Turk, D. Turk, Lysosomal cysteine proteases: facts and opportunities,

EMBO J. 20 (2001) 4629-4633.
[60] J. Deussing, W. Roth, P. Saftig, C. Peters, H.L. Ploegh, J.A. Villadangos, Cathepsins B and D are dispensable for major histocompatibility complex class II-mediated antigen presentation, Proc. Natl. Acad. Sci. USA. 95 (1998) 4516-4521.
[61] S.H. Zhang, R.L. Reddick, J.A. Piedrahita, N. Maeda, Spontaneous hypercholesterolemia and arterial lesions in mice lacking apolipoprotein E, Science 258 (1992) 468-471.
[62] M.H. Moghadasian, B.M. McManus, L.B. Nguyen, S. Shefer, M. Nadji, D.V. Godin, T.J. Green, J. Hill, Y. Yang, C.H. Scudamore, J.J. Frohlich, Pathophysiology of apolipoprotein E deficiency in mice: relevance to apo E-related disorders in humans, FASEB J. 15 (2001) 2623-2630.
[63] W. Shi, X. Wang, J. Wong, C.C. Hedrick, H. Wong, L.W. Castellani, A.J. Lusis, Effect of macrophage-derived apolipoprotein E on hyperlipidemia and atherosclerosis of LDLR-deficient mice, Biochem. Biophys. Res. Commun. 317 (2004) 223-229.
[64] M. Shiomi, T. Ito, The Watanabe heritable hyperlipidemic (WHHL) rabbit, its characteristics and history of development: a tribute to the late Dr. Yoshio Watanabe, Atherosclerosis 207 (2009) 1-7.
[65] E.I. Galanzha, E.V. Shashkov, T. Kelly, J.W. Kim, L. Yang, V.P. Zharov, In vivo magnetic enrichment and multiplex photoacoustic detection of circulating tumour cells, Nat. Nanotechnol. 4 (2009) 855-860.
[66] W.J. Akers, C. Kim, M. Berezin, K. Guo, R. Fuhrhop, G.M. Lanza, G.M. Fischer, E. Daltrozzo, A. Zumbusch, X. Cai, L.V. Wang, S. Achilefu, Noninvasive photoacoustic and fluorescence sentinel lymph node identification using dye-loaded perfluorocarbon nanoparticles, ACS Nano. 5 (2011) 173-182.
[67] K.S. Valluru, J.K. Willmann, Clinical photoacoustic imaging of cancer, Ultrasonography 35 (2016) 267-280.
[68] A. Hannah, G. Luke, K. Wilson, K. Homan, S. Emelianov, Indocyanine green-loaded photoacoustic nanodroplets: dual contrast nanoconstructs for enhanced photoacoustic and ultrasound imaging, ACS Nano 8 (2014) 250-259.
[69] K. Kanazaki, K. Sano, A. Makino, T. Homma, M. Ono, H. Saji, Polyoxazoline multivalently conjugated with indocyanine green for sensitive in vivo photoacoustic imaging of tumors, Sci. Rep. 6 (2016) 33798.
[70] C. Liu, J. Chen, Y. Zhu, X. Gong, R. Zheng, N. Chen, D. Chen, H. Yan, P. Zhang, H. Zheng, Z. Sheng, L. Song, Highly Sensitive MoS2-Indocyanine Green Hybrid for Photoacoustic Imaging of Orthotopic Brain Glioma at Deep Site, Nanomicro. Lett. 10 (2018) 48.

[71] B. Godin, J.H. Sakamoto, R.E. Serda, A. Grattoni, A. Bouamrani, M. Ferrari, Emerging applications of nanomedicine for the diagnosis and treatment of cardiovascular diseases, Trends Pharmacol. Sci. 31 (2010) 199-205.

[72] M.E. Lobatto, V. Fuster, Z.A. Fayad, W.J. Mulder, Perspectives and opportunities for nanomedicine in the management of atherosclerosis, Nat. Rev. Drug Discov. 10 (2011) 835-852.

[73] W.J. Mulder, F.A. Jaffer, Z.A. Fayad, M. Nahrendorf, Imaging and nanomedicine in inflammatory atherosclerosis, Sci. Transl. Med. 6 (2014) 239sr1.

[74] N. DiStasio, S. Lehoux, A. Khademhosseini, M. Tabrizian, The multifaceted uses and therapeutic advantages of nanoparticles for atherosclerosis research, Materials 11 (2018) E754.

[75] J. Levi, S.R. Kothapalli, T.J. Ma, K. Hartman, B.T. Khuri-Yakub, S.S. Gambhir, Design, synthesis, and imaging of an activatable photoacoustic probe, J. Am. Chem. Soc. 132 (2010) 11264-11269.

[76] Y. Wu, S. Huang, J. Wang, L. Sun, F. Zeng, S. Wu, Activatable probes for diagnosing and positioning liver injury and metastatic tumors by multispectral optoacoustic tomography, Nat. Commun. 9 (2018) 3983.